24/PSY/09 NISCHAY RANA

Performance Analysis of PMSG-based Wind Turbine under Normal, Abnormal Grid Conditions and Cyber Attacks

Plagiarism Check

Document Details

Submission ID

trn:oid:::27535:142403991

Submission Date

Jun 10, 2026, 11:28 AM GMT+5:30

Download Date

Jun 10, 2026, 11:32 AM GMT+5:30

File Name

DTU_MTech_Thesis_31_5_26 (1).pdf

File Size

3.3 MB

65 Pages

13,951 Words

72,786 Characters

9% Overall Similarity

The combined total of all matches, including overlapping sources, for each database.

Filtered from the Report

- Bibliography
- Quoted Text
- Cited Text
- Small Matches (less than 10 words)

Match Groups

98 Not Cited or Quoted 9%
Matches with neither in-text citation nor quotation marks

0 Missing Quotations 0%
Matches that are still very similar to source material

0 Missing Citation 0%
Matches that have quotation marks, but no in-text citation

0 Cited and Quoted 0%
Matches with in-text citation present, but no quotation marks

Top Sources

6%	Internet sources
4%	Publications
7%	Submitted works (Student Papers)

Match Groups

98 Not Cited or Quoted 9%
Matches with neither in-text citation nor quotation marks

0 Missing Quotations 0%
Matches that are still very similar to source material

0 Missing Citation 0%
Matches that have quotation marks, but no in-text citation

0 Cited and Quoted 0%
Matches with in-text citation present, but no quotation marks

Top Sources

6%	Internet sources
4%	Publications
7%	Submitted works (Student Papers)

Top Sources

The sources with the highest number of matches within the submission. Overlapping sources will not be displayed.

1	Internet	**powersimtech.com**	<1%
2	Internet	**dspace.dtu.ac.in:8080**	<1%
3	Publication	**Sajeeb Saha, Md Enamul Haque, Md. Apel Mahmud. "Diagnosis and Mitigation of ...**	<1%
4	Internet	**mdpi-res.com**	<1%
5	Student papers	**IIT Delhi on 2014-07-30**	<1%
6	Student papers	**Delhi Technological University on 2019-06-03**	<1%
7	Internet	**orca.cardiff.ac.uk**	<1%
8	Publication	**El-Sayed M. El-Alfy. "Detecting pixel-value differencing steganography using Leve...**	<1%
9	Student papers	**GGS IP University Delhi on 2026-05-24**	<1%
10	Internet	**curve.carleton.ca**	<1%

11	Internet	
	tj.uettaxila.edu.pk	<1%
12	Internet	
	vbn.aau.dk	<1%
13	Student papers	
	University of Northumbria at Newcastle on 2026-05-11	<1%
14	Publication	
	Btissam Majout, Badre Bossoufi, Mohammed Karim, Paweł Skruch, Saleh Mobaye...	<1%
15	Student papers	
	University of Northumbria at Newcastle on 2022-01-06	<1%
16	Publication	
	Zhen Wang, Xianggen Yin, Yu Chen. "Model Predictive Arm Current Control for M...	<1%
17	Internet	
	dspace.univ-ouargla.dz	<1%
18	Internet	
	www.ijltemas.in	<1%
19	Student papers	
	GGS IP University Delhi on 2026-05-29	<1%
20	Student papers	
	Loyola University, Chicago on 2026-06-06	<1%
21	Publication	
	Mutaz Alanazi, Abdulhakeem Alsaleem, Ahmed A. Mahfouz. "Modeling, Simulatio...	<1%
22	Student papers	
	Stefan cel Mare University of Suceava on 2011-08-14	<1%
23	Student papers	
	University of Newcastle upon Tyne on 2013-04-17	<1%
24	Student papers	
	University of Sheffield on 2016-06-23	<1%

25	Internet	
data.epo.org		<1%
26	Internet	
eprints.soton.ac.uk		<1%
27	Internet	
media.neliti.com		<1%
28	Internet	
www.arrakis.nl		<1%
29	Internet	
www.eng.mu.edu		<1%
30	Internet	
www.ijcee.org		<1%
31	Internet	
www.mdpi.com		<1%
32	Student papers	
Amity University on 2016-07-26		<1%
33	Publication	
Energy Systems, 2013.		<1%
34	Student papers	
IIT Delhi on 2014-05-05		<1%
35	Student papers	
RMIT University on 2016-10-12		<1%
36	Student papers	
The University of Manchester on 2013-09-02		<1%
37	Student papers	
University of Newcastle upon Tyne on 2010-08-31		<1%
38	Student papers	
University of Stellenbosch, South Africa on 2011-02-02		<1%

39	Internet	
dokumen.pub		<1%
40	Internet	
dspace.nitrkl.ac.in		<1%
41	Internet	
eprints.utas.edu.au		<1%
42	Internet	
open.uct.ac.za		<1%
43	Internet	
www.bestpfe.com		<1%
44	Internet	
www.ijettjournal.org		<1%
45	Internet	
www.jetir.org		<1%
46	Student papers	
ABV-Indian Institute of Information Technology and Management Gwalior on 201...		<1%
47	Student papers	
AUT University on 2026-06-08		<1%
48	Student papers	
Brunel University on 2013-02-08		<1%
49	Student papers	
Deakin University on 2019-06-17		<1%
50	Student papers	
Glasgow Caledonian University on 2023-09-13		<1%
51	Publication	
Sureshbhai, Patel Krishna. "Performance Investigation and Protection of Grid Con...		<1%
52	Student papers	
The University of Manchester on 2012-08-30		<1%

53	Student papers	The University of Manchester on 2015-08-31	<1%
54	Student papers	Universiti Teknologi Malaysia on 2011-05-07	<1%
55	Publication	Yingchun Yue, Tao Ye. "Predicting precipitable water vapor by using ANN from G...	<1%
56	Publication	Yizhen Wang, Zhiqian Wang, Hao Sheng. "Optimizing wind turbine integration in ...	<1%
57	Student papers	iGroup on 2014-06-19	<1%
58	Internet	knowledgecommons.lakeheadu.ca	<1%
59	Publication	Chinchilla, M.. "Power limits of grid-connected modern wind energy systems", Re...	<1%
60	Publication	Davide Cittanti, Matteo Gregorio, Eugenio Bossotto, Fabio Mandrile, Radu Bojoi. "...	<1%
61	Student papers	Engineering Institute of Technology on 2025-11-17	<1%
62	Student papers	Jawaharlal Nehru Technological University on 2025-05-20	<1%
63	Publication	Mendis, Nishad, Saad Sayeef, Kashem M. Muttaqi, and Sarath Perera. "Hydrogen ...	<1%
64	Student papers	Nazarbayev University on 2024-07-30	<1%
65	Student papers	Panjab University on 2014-03-29	<1%
66	Publication	Taheni Swibki, Ines Ben Salem, Lilia El Amraoui. "Modeling and control of direct-d...	<1%

67	Student papers	
The University of Manchester on 2010-09-02		<1%
68	Student papers	
The University of the South Pacific on 2026-05-07		<1%
69	Student papers	
University of Leeds on 2020-09-09		<1%
70	Student papers	
University of Liverpool on 2015-05-06		<1%
71	Student papers	
University of Liverpool on 2025-04-30		<1%
72	Student papers	
University of Newcastle upon Tyne on 2013-07-29		<1%
73	Student papers	
University of Newcastle upon Tyne on 2015-08-04		<1%
74	Student papers	
University of Technology, Sydney on 2015-05-01		<1%
75	Student papers	
Visvesvaraya National Institute of Technology on 2022-09-09		<1%
76	Internet	
docplayer.net		<1%
77	Internet	
epdf.tips		<1%
78	Internet	
fr.scribd.com		<1%
79	Internet	
link.springer.com		<1%
80	Internet	
m.moam.info		<1%

81 Internet	
vtechworks.lib.vt.edu	<1%
82 Internet	
www.tntech.edu	<1%

Performance Analysis of PMSG-based Wind Turbine under Normal, Abnormal Grid Conditions and Cyber Attacks

A DISSERTATION

SUBMITTED IN PARTIAL FULFILLMENT OF THE REQUIREMENTS FOR
THE AWARD OF THE DEGREE OF

MASTER OF TECHNOLOGY

IN

POWER SYSTEMS

Submitted by:
NISCHAY RANA

24/PSY/09

Under the supervision of

PROF. ALKA SINGH

DR. SHATAKSHI

DEPARTMENT OF ELECTRICAL ENGINEERING
DELHI TECHNOLOGICAL UNIVERSITY
(Formerly Delhi College of Engineering)
Bawana Road, Delhi-110042

June, 2026

ABSTRACT

The integration of Permanent Magnet Synchronous Generator (PMSG) wind turbine into the modern power grid demands strict the Low Voltage Ride Through (LVRT) compliance and robust cyber-physical security. Convectional Proportional-Integrator (PI) controllers exhibit limited transient response during deep voltage sags. To overcome these limitations, this dissertation proposed and implemented an Artificial Neural Network (ANN) based LVRT control strategy for Grid Side Converter (GSC). This dissertation also deeply studies the impact and analyses the severity of cyber-attacks such as Fault Data Injection (FDI), Denial-of-Service (DoS), Replay and Control Parameter attacks on the system.

Simulations in MATLAB/Simulink demonstrated that the data driven ANN controller effectively suppressed DC-link overvoltage and dynamically injects reactive power, extending the system's voltage sag tolerance from 20% under conventional control to 40%. Finally, the computational feasibility, execution speed and real-world applicability of the proposed control architecture were successfully validated using an OPAL-RT real time digital simulator.

CONTENTS

CHAPTER 1: INTRODUCTION

CHAPTER 2: LITERATURE REVIEW

CHAPTER 3: MATHEMATICAL MODELLING OF WECS

LIST OF TABLES

LIST OF FIGURES

LIST OF SYMBOLS, ABBREVIATIONS AND NOMENCLATURE

- **PMSG:** Permanent Magnet Synchronous Generator
- **DFIG:** Doubly-Fed Induction Generator
- **WECS:** Wind Energy Conversion System
- **MSC:** Machine Side Converter
- **GSC:** Grid Side Converter
- **FOC:** Field Oriented Control
- **VOC:** Voltage Oriented Control
- **MPPT:** Maximum Power Point Tracking
- **PLL:** Phase Locked Loop
- **PWM:** Pulse Width Modulation
- **IEGC:** Indian Electricity Grid Code
- **CEA:** Central Electricity Authority
- **GWEC:** Global Wind Energy Council
- $\mathbf{P_m}$: Mechanical Power (W)
- $\mathbf{C_p}$: Power Coefficient
- $\boldsymbol{\lambda}$: Tip Speed Ratio
- $\boldsymbol{\beta}$: Pitch Angle (degrees)
- $\boldsymbol{\rho}$: Air Density ($1.215 \mathrm{kg/m^3}$)
- **v:** Wind Speed (m/s)
- **R:** Rotor Radius (m)
- **A:** Swept Area ($\mathrm{m^2}$)
- $\mathbf{d-q}$: Direct and Quadrature axis
- $\mathbf{V_{dc}}$: DC Link Voltage (V)
- $\boldsymbol{\omega_m}$: Mechanical angular speed (rad/s)
- $\boldsymbol{\omega_e}$: Electrical angular speed (rad/s)
- $\mathbf{T_e}$: Electromagnetic Torque (Nm)
- $\mathbf{T_m}$: Mechanical Torque (Nm)
- $\mathbf{L_d, L_q}$: d-axis and q-axis Inductances (H)
- $\mathbf{R_s}$: Stator Resistance (Ω)
- $\boldsymbol{\psi_f}$: Permanent Magnet Flux Linkage (Wb)

CHAPTER 1

INTRODUCTION

1.1 GENERAL BACKGROUND

The global transition toward sustainable energy has accelerated the integration of renewable energy sources into modern power grids. The integration of large-scale intermittent renewable energy sources imposes many difficulties in maintaining grid stability and reliability [1-4]. Wind energy is really in the spotlight these days, here it's not just promising, it's booming. The Permanent Magnet Synchronous Generator (PMSG) is the excellent choice for modern multi-megawatt wind turbines due to the absence of the gearbox unlike Doubly-Fed Induction Generators (DFIGs). Due to which PMSG has fewer mechanical losses, less maintenance costs and a less failure rate then DFIG. PMSG systems also utilize full-scale power converters, which means that the generator and the grid operate independently. This configuration provides better control of active and reactive power, high power density and performance during faults [5-16].

1.2 LOW VOLTAGE RIDE THROUGH (LVRT) AND GRID CODE COMPLIANCE

As wind energy makes up a larger share of the global power grid, the sudden loss of large wind farms during network faults becomes a real threat to grid stability, it can even trigger power outages that ripple through the whole system. To avoid this, transmission system operators apply strict technical specifications, so-called Grid Codes. Those codes describe exactly how a power plant must behave, and what parameters it must meet, to keep the grid running safely and reliably. The Low Voltage Ride Through (LVRT) capability is one of the main and most demanding specifications imposed in these codes [17]. LVRT rules states that wind turbines must stay connected during a voltage sag and should provide reactive power to support to the grid for its recovery.

1.2.1 The Indian Electricity Grid Code and CEA Standards [18]

In India, renewable energy generators and their connection to the grid are directly regulated by the Central Electricity Regulatory Commission (CERC) through the Indian Electricity Grid Code (IEGC) 2023 and Central Electricity Authority (CEA) Technical Standards for Connectivity to the Grid. The growth of India's renewable energy sector, these codes were updated to address the issue of reduced system inertia, owing to the replacement of conventional synchronous generators with inverter-based systems such as PMSG wind turbines.

To connect wind energy systems to the Indian inter-state transmission system (ISTS), they need to comply with a number of critical technical benchmarks at the Point of Interconnection (POI):

- Voltage Ride Through (LVRT & HVRT): As per the guidelines by CEA, no disconnection of wind farms above 66 kV shall take place in case of the occurrence of predetermined voltage dips. These wind farms should quickly react to the event, detect fault, and deliver reactive current to maintain voltage until protective relays rectify the problem.
- Reactive Power Compensation: The converters of the wind turbines must have capability to deliver reactive power according to demand while having a power factor of ±0.95.
- Frequency Ride Through: Stable operation is mandated for the system even if the frequency varies between 47.5 Hz and 52 Hz. Active participation in primary frequency control is also demanded from the plant.
- Active Power Regulation: It is recommended that the CEA plants reduce their load slowly to avoid any immediate disturbances in the grid. This should not exceed 10 percent per minute.

1.2.2 Demerits of Conventional LVRT Methodologies

PMSG systems, with their full-scale back-to-back converters, offer a platform for managing faults. But meeting India's strict LVRT and reactive power criteria is still a tough control problem. Industry usually leans on extra equipment like Static VAR Compensators (SVC) or

STATCOMs to supply reactive power during grid trouble [19-22]. While these work, they come at a steep cost and make the whole system more complex. Conventional LVRT methods built into the turbine often depend on hardware tweaks, braking choppers or active crowbar circuits paired with basic Proportional-Integral (PI) control schemes. But there are clear downsides. Hardware methods dump extra active power as heat, which wastes energy and puts harsh thermal stress on converter parts. The standard PI controllers, tuned for certain fixed conditions, falter when faced with the non-linear, fast-changing scenarios that come with deep voltage dips. As a result, response slows down, reactive power support falls short of CEA curve requirements, and DC-link overvoltages remain a risk. This highlights the urgent need for smarter GSC control solutions that meet grid code requirements by moving beyond rigid PI loops and costly external hardware [23-25].

The presence of full-scale back-to-back converters makes PMSG a good platform for fault management. Still, meeting the strict standards set by India regarding LVRT and reactive power remains a control issue. Traditionally, the industry has employed additional equipment, for example, Static VAR Compensator or STATCOM, to provide reactive power in the event of grid disturbances [19–22]. Although this method works well but it cost extra on the system. Traditional LVRT schemes employed by the wind turbine are hardware-based schemes where braking choppers or active crowbars combined with PI control. However, there are disadvantages to employing this approach. Firstly, the hardware-based solution causes active power dissipation in the form of energy, which not only causes a loss of power but is also an enormous burden on the converter. Secondly, since traditional PI controllers work best under static circumstances, their operation during sudden voltage sags is relatively poor. This causes delays, resulting in failure to provide required reactive power in time to comply with the CEA curve, among other difficulties. All this demonstrates the necessity for advanced GSC control methods, which go beyond the traditional hardware schemes and PI controllers.

1.3 CYBER-PHYSICAL VULNERABILITIES IN WIND ENERGY SYSTEMS

Increasing development of modern power systems has a combination of the physical electrical network and a complex communication system has been achieved. At present, the cyber security of wind turbines has become more vulnerable because of cyber intrusion, which can be aimed at causing damage to the wind turbine control layer of the infrastructure. Intrusion in the system can significantly reduce the overall performance of the system and may lead to a cascade effect [26-30]. The wind turbines using permanent magnet synchronous generators (PMSG) rely on fast data exchange between sensors monitoring grid voltage, rotor speed, and DC-link voltage and central control unit controlling the converters. Advanced and stealthy cyber intrusions make abnormal behaviour and patterns harder to distinguish from standard system failures [33-35].

In the described system, there are several types of cyber intrusion that require additional attention and analysis due to their prevalence and potential impacts on wind turbine operation: False Data Injection (FDI), Denial-of-Service (DoS), Replay, and Control Parameter. Specifically, FDI intrusion aims to introduce harmful data in the process of feedback loop, while DoS intrusion tries to exhaust resources by interrupting communication channel and commands for converter control [36, 37]. Replay attacks involve collecting of authentic information about grid condition through sensors and its further resubmission to the controller in order to disguise the actual condition of the grid [38]. Finally, Control Parameter attack implies penetration into the memory of the controller and altering of internal parameters of controllers, including changes in PI regulator gains [39].

7

Any of the listed types of cyber-attack would result in misleading of the controller as to the actual state of the grid. For instance, a false data intrusion might provoke an unneeded LVRT response, or it can mask grid fault making the turbine unable to provide sufficient reactive power support. Thus, it is necessary to conduct an investigation to assess the dynamic effects of cyber intrusions on control of PMSG wind turbines.

19

1.4 OBJECTIVES OF THE DISSERTATION

The specific objectives of this dissertation are to:

1. Develop system models: The development of detailed mathematical models and simulations of the PMSG wind energy conversion system will be used for dynamic analysis under variable aerodynamic conditions.
2. Evaluate the Limitations of Conventional Control: Analyse and assess the constraints

in the use of conventional PI control techniques for the grid-integrated system due to their slow transient response and poor LVRT control capability.

3. Implement intelligent control: Designing and implementing an intelligent ANN control scheme for LVRT control of the GSC to rapidly suppress the excessive rise in the DC-link voltage.
4. Assess Vulnerabilities: The assessment of vulnerabilities in the cyber-physical system will entail developing dynamic models for false data injection (FDI), DoS, replay attacks, and control parameter attacks on wind turbine stability.
5. Validate system resiliency: The validity of the proposed ANN controller will be validated in terms of its physical fault tolerance and resiliency using MATLAB/Simulink and OPAL-RT simulations.

1.5 ORGANIZATION OF THE DISSERTATION

The dissertation is sequentially organized to present the research work systematically:

- **Chapter 2: Literature Review** presents a comprehensive literature review outlining the current state of research in PMSG modelling, LVRT methodologies, and grid cybersecurity.
- **Chapter 3: Mathematical Modelling of System** details the mathematical modelling and control strategy of the PMSG system.

- **Chapter 4: Modelling and Control Schemes** elaborates on the design of the MSC and GSC control.

- **Chapter 5: Results and Simulation** present the simulation done in MATLAB/Simulink 2024a and their experimental validation carried out on OPAL-RT platform.

CHAPTER 2

LITERATURE REVIEW

2.1 INTRODUCTION

In this chapter, we explore the incorporation of renewable energy systems into today's energy networks, concentrating on wind energy systems, and discuss the need for advanced control mechanisms and strong communication networks. In normal situations, these controllers employ complicated control algorithms to ensure maximum power production from wind and achieve system synchronization. In exceptional situations where voltage sags and short-circuits occur, there arises the need for instant action using sophisticated protection processes such as LVRT. Digital technology not only improves the efficiency of the power generation process but also increases fault tolerance. However, the adoption of digital technology in power generation has also made the existing grid structure more susceptible to attacks. The modern-day turbine utilizes a lot of digitized sensing information to detect significant events making it susceptible to various cyber-attacks. In particular, the communication network can be exploited by attackers to inject, manipulate, distort, or hide important events. In this chapter, we discuss previous works concerning permanent magnet synchronous generators-based wind energy conversion systems, their control techniques, and the cyber-attack vulnerabilities that arise due to the use of digitization technology. The four main types of cyber-attacks discussed here include FDI, DoS, replay attacks, and control parameter attacks.

2.2 PMSG-BASED WIND ENERGY CONVERSION SYSTEMS [5-11]

PMSGs outperform traditional systems such as DFIGs. Academic research explains this in terms of PMSGs' superior performance in low and varying wind speeds, lighter weight, and fewer maintenance needs due to the lack of gearbox prone to breakdowns. Moreover, PMSGs demonstrate improved power generation and economics over time. Additional advantages of using PMSGs compared to DFIGs include the following:

- Stability: The PMSG system showed no instability during rapid wind changes, unlike DFIGs which can suffer from rotor current spikes.
- Control: FOC and VOC approaches allow for controlling torque and power factor independently of each other, a task more difficult to accomplish for DFIGs because of interaction between stator and rotor fluxes;
- Maintenance: While simulation was not employed in this research, the absence of slip rings from the analysed PMSG suggests considerable reduction in long-term maintenance expenditures compared to a similar DFIG.

PMSG wind turbines connect to the grid using a full B2B converter topology that completely eliminates a direct connection between the generator and the grid. As can be seen in Figure 5.3.1, it includes a machine side converter (MSC) and a grid side converter (GSC) separated by a DC-link capacitor. [7] highlights that such topology demonstrates remarkable stability and resilience in the face of harsh winds.

PMSGs allow for employing complex control strategies related to advanced electronics. [11] outline the control strategy as involving two separate control units: the role of the MSC is to adjust the generator speed (ω_m) to achieve MPPT by manipulating its torque. It is usually done through vector control of rotor flux (using d-axis) and allowing independent control of electromagnetic torque (i_{sq}) and magnetic flux (i_{sd}).

7 On the other hand, the primary goals of the GSC are to ensure stability of DC-link voltage (V_{dc}) to control power flow to the grid and adjust reactive power (Q_g) transmitted to the grid. According to the literature, this can be best done through vector control with respect to the grid voltage and synchronized using a PLL. With the help of an external DC voltage loop and fast inner current loops, it is possible to perform stable power conversion, provide dynamic reactive power for grid services, or operate at unity power factor.

2.3 VULNERABILITIES IN WIND FARM CONTROL ARCHITECTURES [11-16]

While most early cybersecurity research concentrated on grid level vulnerabilities, the focus is now shifting towards inverter-based devices such as PMSG wind turbines. [13] Recent penetration tests and impact studies show how open wind farms are really vulnerable to network breaches. Moreover, recent studies investigate the influence of attacks on wind generation on inter-area oscillation damping of entire power systems [16]. These turbines are very much exposed to the fast interlinked control loops completely depending on valid sensor data (e.g. grid voltage, rotor speed and DC-link voltage) and command signals. “If the attacker understands how the control functions, they can bypass traditional security and go immediately to the stability of the turbine.” For example, hits to offshore wind farms connected to HVDC have severe risks to grid-following converters.

2.4 GRID INTEGRATION STANDARDS AND CHALLENGES [17-20]

Renewable grid integration has become a completely different game in the past decade. Initially, the policy was to allow wind turbines to connect and then disconnect them whenever there was any failure so that no damage would occur on them. However, due to grid inertia being reduced due to the increasing number of inverter-based technologies, wind turbines now have to participate actively in maintaining grid integrity.

As far as India is concerned, CERC has increased its expectations from wind generators by introducing amendments in the Indian Electricity Grid Code (IEGC):

- Indian Electricity Grid Code (IEGC) 2024: Amendments made by CERC lead to stricter requirements.
- Reactive Power: The generators will be required to produce dynamic reactive power and keep voltage fluctuation in the range of ±5%.
- Frequency Response: Primary Frequency Response (droop control) of turbine needs to be provided.
- Harmonics: Limits of THD (IEEE 519) necessitate the use of LCL or tuned filters.

Numerous research studies support the application of Voltage Oriented Control (VOC) in the GSC, which is the preferred method because independent control over d-axis and q-axis is possible.

2.5 CYBER-PHYSICAL SYSTEMS (CPS) AND GRID SECURITY CHALLENGES [25-30]

Today’s PMSG wind turbines are no longer just machines. They are complete Cyber-

Physical Systems, incorporating hardware, real-time controllers, large sensor networks and communication layers such as SCADA. This digital integration is essential for advanced grid support, such as LVRT, but it also opens up a whole new range of threats. Researchers have expressed major concern with the security of the CPS of the electric grid. CPS security surveys highlight that a cyberattack on operational technology (OT) is not the same as the usual IT breaches and affects the physical world directly. The fallout can mean broken equipment, financial losses or even major blackouts. The 2015 cyber-attack on Ukraine's grid showed just how dangerous these vulnerabilities really are in critical OT setups.

2.6 RESEARCH GAPS IDENTIFIED

Despite advances in PMSG turbine modelling and analysis of grid cybersecurity, several gaps become apparent after careful review of the latest literature concerning the synergy between dynamic fault ride-through and cyber-resilience of the turbines:

1. Rigidness of Conventional LVRT Controllers: Most studies related to overcoming LVRT challenges in PMSG turbines tend to use conventional PI controllers and solutions that involve the use of extra hardware, such as STATCOM or crowbar. The drawback of the latter solution is the rigidity and limited capacity to compensate for rapid voltage swings in the case of severe conditions. Data-dependent control loops capable of tuning based on the level of the fault must be researched.
2. Isolated Focus on Cyber-Security: In actual, there is insufficient attention to the physical effects of attacks like Replay, FDI on the converters' control loops (GSC and MSC) and subsequent fault response of the turbine itself.
3. Lack of Comprehensive Cyber-Resilient Control Strategies: Grid fault management (LVRT) and cyberattack detection are two distinct topics. Most defences are software-based anomaly detectors that alert operators, but do not actively stabilize the turbines. The real gap is in unified architectures such as ANN that can boost reactive power during faults and filter out corrupted data at the same time.

CHAPTER 3

MATHEMATICAL MODELLING OF WECS

3.1 INTRODUCTION [5-7]

A robust control system relies on a precise mathematical representation of the physical system. This chapter derives the dynamic equations for the 4MW PMSG based wind turbine system. The modelling philosophy follows the d-q reference frame theory, which simplifies the control of three-phase AC machines by transforming time-varying quantities into DC equivalents. Fig. 3.1 shows the schematic diagram of the proposed PMSG wind turbine system.

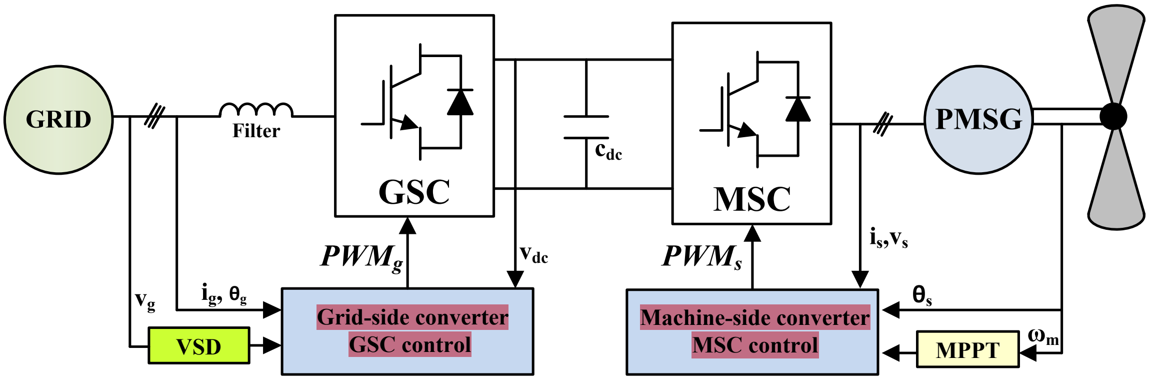

Fig. 3.1. Wind energy integration system diagram

3.2 AERODYNAMIC MODELLING OF WIND TURBINE [8-9]

The wind turbine rotor is the prime mover, converting the kinetic energy of the wind into mechanical torque. The power available in the wind (P_{wind}) passing through an area A is given by the kinetic energy flux:

$$P_{wind} = \frac{1}{2}\rho A v^3 \tag{3.1}$$

where $\rho = 1.215\,kg/m^3$ (Air density), $R = 54\,m$ (Rotor radius for 4 MW turbine), $A = \pi R^2 \approx 9160\,m^2$ (Swept area), v is the wind speed (m/s).

The mechanical power captured by the turbine (P_m) is a fraction of this available power, as shown in Fig. 3.2 and defined by the Power Coefficient (C_p):

$$P_m = C_p(\lambda,\beta)P_{wind} = \frac{1}{2}\rho A C_p(\lambda,\beta)v^3 \tag{3.2}$$

C_p is not a constant but a non-linear function of λ and the blade pitch angle β. It represents the aerodynamic efficiency. According to the Betz limit, the theoretical maximum $\mathrm{C_p}$ is $16/27 \approx 0.593$. Practical turbines achieve 0.45 - 0.50.

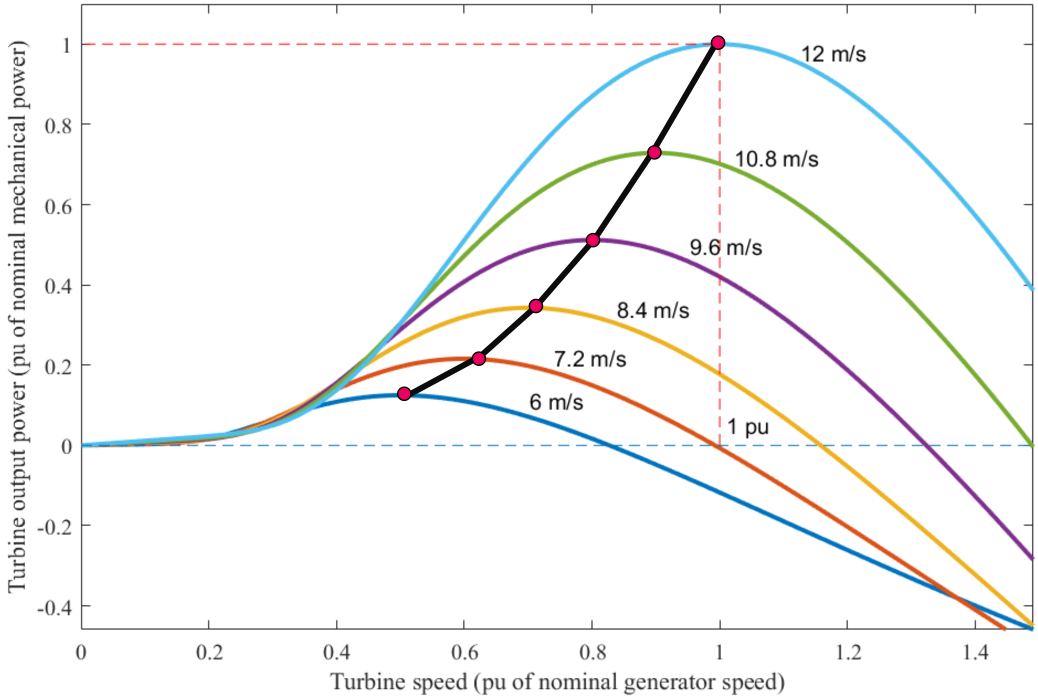

Fig. 3.2. Wind turbine power curves at different wind speeds.

Tip Speed Ratio (TSR):

The aerodynamic efficiency depends critically on the Tip Speed Ratio (λ), which is the ratio of the blade tip speed to the wind speed:

$$\lambda = \frac{\omega_m R}{v} \tag{3.3}$$

where ω_m is the mechanical angular velocity of the rotor (rad/s).

This dissertation utilizes the standard numerical approximation for C_p often used in IEEE literature [11]:

$$C_p(\lambda,\beta) = c_1\left(\frac{c_2}{\lambda_i} - c_3\beta - c_4\right)e^{-\frac{c_5}{\lambda_i}} + c_6\lambda \tag{3.4}$$

With the intermediate variable λ_I defined as:

$$\frac{1}{\lambda_i} = \frac{1}{\lambda + 0.08\beta} - \frac{0.035}{\beta^3 + 1} \tag{3.5}$$

The coefficients used are: $c_1 = 0.5176$, $c_2 = 116$, $c_3 = 0.4$, $c_4 = 5$, $c_5 = 21$, $c_6 = 0.0068$. when $\beta = 0°$. Fig. 3.3 gives us the characteristic curve between the λ and C_p, where C_p is maximized ($C_p = 0.41$) at a specific λ , which is $\lambda = 5.6$.

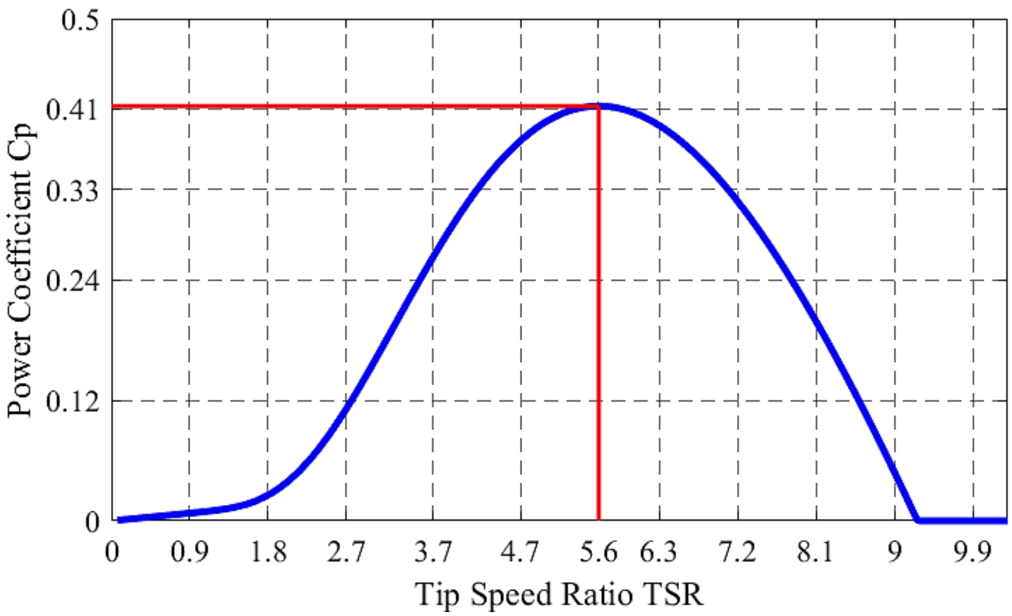

Fig. 3.3. Tip Speed Ratio (λ) vs Power Coefficient (C_p) curve.

Aerodynamic Torque:

The mechanical torque (T_m) exerted on the shaft is derived from the power:

$$T_m = \frac{P_m}{\omega_m} = \frac{1}{2}\rho\pi R^5 C_p(\lambda, \beta)\frac{v^3}{\lambda R} \cdot \frac{1}{v/\lambda} \tag{3.6}$$

Simplifying using $\omega_m = \lambda v/R$:

$$T_m = \frac{1}{2}\rho\pi R^3 v^2 \frac{C_p(\lambda,\beta)}{\lambda} \tag{3.7}$$

This equation shows that for a given wind speed, torque can be controlled by varying the rotor speed, which affects λ or by pitch angle (β).

3.3 MECHANICAL DRIVE TRAIN MODELLING [9]

The driven train transmits torque from the rotor to the generator. For PMSG system, the absence of a gearbox simplifies the dynamics. However, the system still possesses inertia and damping.

Single-Mass Model:

For the purpose of electrical control design, a single-mass lumped parameter model is sufficient and is widely used in literature. The equation of motion (Swing Equation) is:

$$J_{eq}\frac{d\omega_m}{dt} = T_m - T_e - B\omega_m \tag{3.8}$$

where:

- J_{eq}: Equivalent total inertia ($kg \cdot m^2$). For a 4 MW turbine, this value is significant (approx. $10{,}000 + kg \cdot m^2$).
- T_e: Electromagnetic braking torque from the generator ($N \cdot m$).
- B: Viscous friction coefficient representing aerodynamic drag and bearing friction.

This differential equation 3.8 models the acceleration of the rotor. When $T_m > T_e$, the rotor accelerates, storing kinetic energy. The control system regulates T_e to manage speed.

3.4 MODELLING OF PMSG [10-11]

The PMSG is a multiphase AC machine. Modelling it in the stationary abc frame is complex due to time-varying inductances. Park's Transformation is used to convert to a synchronous rotating $d - q$ reference frame, where variables appear as DC quantities in steady state.

34

Reference Frame Transformations:

1. Clarke Transformation ($abc\ to\ \alpha\beta$): Converts 3-phase quantities to a 2-phase stationary frame.
2. Park Transformation ($\alpha\beta\ to\ dq$): Rotates the frame at the electrical speed ω_e to align with the rotor flux.

68

Electrical Dynamics in d-q Frame are discussed in(3.9-3.14):

The stator voltage equations in the rotor flux reference frame are derived as:

65

$$V_{sd} = R_s i_{sd} + \frac{d\psi_{sd}}{dt} - \omega_e \psi_{sq} \tag{3.9}$$

$$V_{sq} = R_s i_{sq} + \frac{d\psi_{sq}}{dt} + \omega_e \psi_{sd} \tag{3.10}$$

where flux linkages are:

$$\Psi_{sd} = L_d i_{sd} + \psi_f \tag{3.11}$$

$$\Psi_{sq} = L_q i_{sq} \tag{3.12}$$

Substituting flux equations into voltage equations:

$$V_{sd} = R_s i_{sd} + L_d \frac{di_{sd}}{dt} - \omega_e L_q i_{sq} \tag{3.13}$$

$$V_{sq} = R_s i_{sq} + L_q \frac{di_{sq}}{dt} + \omega_e L_d i_{sd} + \omega_e \psi_f \tag{3.14}$$

Electromagnetic Torque:

The torque produced by the PMSG is:

$$T_e = \frac{3}{2} N_p \left(\psi_{sd} i_{sq} - \psi_{sq} i_{sd} \right) \tag{3.15}$$

Substituting flux linkages:

$$T_e = \frac{3}{2} N_p \left[\psi_f i_{sq} + \left(L_d - L_q \right) i_{sd} i_{sq} \right] \tag{3.16}$$

For a Surface-Mounted PMSG (SPM), the d and q axis inductances are equal ($L_d = L_q$). The reluctance torque term vanishes, yielding a linear relationship between torque and q-axis current:

$$T_e = \frac{3}{2} N_p \psi_f i_{sq} \tag{3.17}$$

This linearity is the key advantage exploited by Field Oriented Control.

3.5 MODELLING OF POWER CONVERTERS AND DC LINK [12-5]

The B2B converter consists of two 2-level Voltage Source Converters (VSC) utilizing IGBTs.

DC Link Dynamics is discussed using the energy stored in capacitor:

The DC link capacitor acts as an energy buffer. Its voltage dynamics are governed by the power balance:

$$P_{dc} = P_{msc} - P_{gsc} \tag{3.18}$$

$$V_{dc} C_{dc} \frac{dV_{dc}}{dt} = P_{msc} - P_{gsc} \tag{3.19}$$

where P_{msc} is active power from the generator and P_{gsc} is active power delivered to the grid. To maintain constant V_{dc}, the grid side converter must export exactly the amount of active power being generated.

3.6 GRID FILTER DESIGN [16]

The GSC is connected to the grid via a filter to smooth the PWM output. An RL filter (Grid Resistance R_g and Grid Inductance L_g) is modelled. The voltage balance across the filter in the grid-voltage oriented $\mathrm{d-q}$ frame is:

$$V_{inv\_d} = V_{grid\_d} + R_g i_{gd} + L_g \frac{di_{gd}}{dt} - \omega_g L_g i_{gq} \tag{3.20}$$

$$V_{inv\_q} = V_{grid\_q} + R_g i_{gq} + L_g \frac{di_{gq}}{dt} + \omega_g L_g i_{gd} \tag{3.21}$$

These equations reveal a cross-coupling between the d and q axes (terms with $\omega_g L_g$), which must be decoupled in the control design.

The Table 3.1 summarises the modelling of PMSG-WECS using the designing equations.

TABLE 3.1: SUMMARY OF GOVERNING MATHEMATICAL EQUATIONS FOR PMSG-WECS COMPONENTS

System Component	Parameter Modelled	Governing Equation
Wind Turbine Aerodynamics	Mechanical Power Extracted (P_m)	$P_m = C_p(\lambda,\beta)P_{wind} = \frac{1}{2}\rho A C_p(\lambda,\beta)v^3$
	Power Coefficient ($C_p(\lambda,\beta)$)	$C_p(\lambda,\beta) = c_1\left(\frac{c_2}{\lambda_i} - c_3\beta - c_4\right)e^{-\frac{c_5}{\lambda_i}} + c_6\lambda$
	Tip Speed Ratio (λ)	$\lambda = \frac{\omega_m R}{v}$
	Mechanical Torque (T_m)	$T_m = \frac{1}{2}\rho\pi R^3 v^2 \frac{C_p(\lambda,\beta)}{\lambda}$
DC-Link Dynamics	DC-Link Voltage variation (V_{dc})	$V_{dc}C_{dc}\frac{dV_{dc}}{dt} = P_{msc} - P_{gsc}$

3.7 CONCLUSION

In this chapter, the complete mathematical modelling and control architecture of grid-connected PMSG wind energy conversion system was discussed. Some for the fundamental aerodynamic equations, along with the detailed vector control schemes for the MSC to achieve maximum power extraction, and the GSC to manage DC-link voltage and reactive power, were thoroughly discussed. Furthermore, these theoretical formulations were successfully implemented within the MATLAB/Simulink environment, establishing a robust and fully operational baseline model. This high-fidelity simulation model provides the critical foundation for the subsequent chapter, where it will be utilized as a dynamic testbed to evaluate the system's LVRT performance under severe grid faults and analyse its vulnerabilities against sophisticated cyber-physical attacks.

CHAPTER 4

MODELLING OF CONTROL SCHEMES

4.1 INTRODUCTION [5-8]

Following the mathematical modelling established previously, this chapter looks at how the control systems for the PMSG wind energy conversion system handle both normal and abnormal operations. To test how stable the system is, the chapter examines its control strategies in three main scenarios:

1. Normal Operation of MSC and GSC: Here we run the system under steady state conditions and evaluating baseline control loop performance. MSC is assessed over the ability of tracing maximum power and GSC is tested for its ability of exporting smooth active power, stable DC-link voltage and keeping power factor lose to unity.

2. LVRT Compliance, Grid Codes and ANN implementation: since standard PI controllers often reacts too slow during severe, non-liners faults, an ANN based LVRT method is discussed. This approach adapts the grid side current reference accurately and keeps DC-link stable, making sure the system sticks to grid code compliance guidelines.

3. Cyber-Attack Analysis: The wind turbine operates at a CPS, making its communication network and sensors feedback lines vulnerable to cyber-attacks. This section models four typer of attacks like FDI, DoS, Replay and Control Parameter attacks.

By simulating these three scenarios, the chapter gives a thorough look at the PMSG control architecture featured in Fig. 4.1, showing how it performs under real-world grid faults and how it is most exposed to cyber-attack risks.

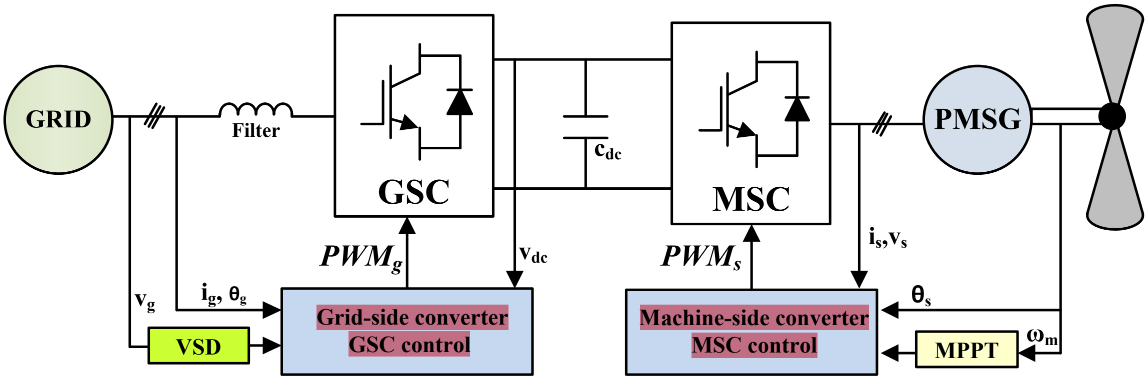

Fig. 4.1. Wind energy integration system diagram

4.2 MACHINE SIDE CONTROL (MSC) STRATEGY [8-10]

The MSC operates as a rectifier/driver for the generator. Its primary control objective is to regulate the electromagnetic torque T_e to control the rotor speed ω_m for MPPT. Fig. 4.2 shows the block diagram of MSC.

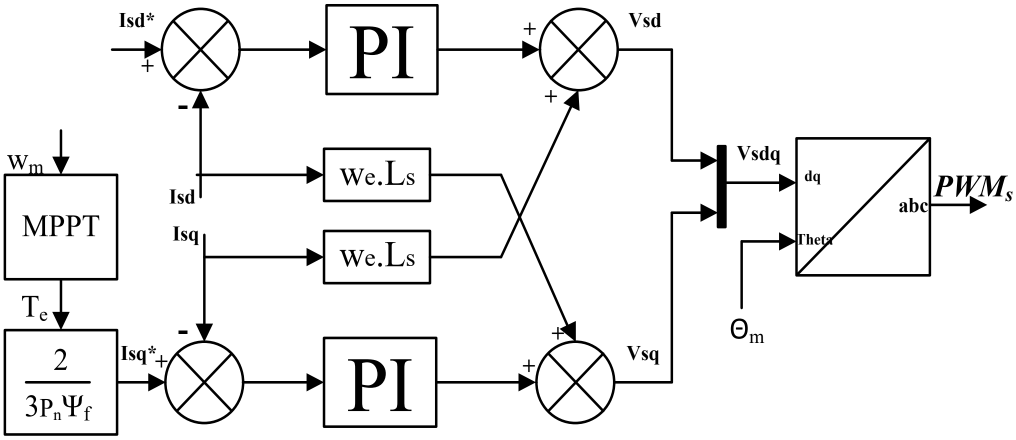

Fig. 4.2. Machine side control scheme block.

4.2.1 Maximum Power Point Tracking (MPPT) Logic

In order to achieve Maximum Power Point Tracking (MPPT) for a given wind speed, the MSC controller depicted in Fig. 4.2 primary objective is to regulate the generator speed (ω_m). This is accomplished by employing the (4.1):

$$T_e = \frac{1}{2}\rho A C_p(\lambda, \beta)\left(\frac{w_m R}{\lambda}\right)^3 \Big/ w_m \tag{4.1}$$

The control strategy calculates the optimal torque reference T_e^* based on the measured rotor speed squared. This OTC method is sensor less regarding wind speed (no anemometer required for the loop), making it robust and reliable.

4.2.2 Field Oriented Control (FOC) Implementation

Fig. 4.2 shows the implementation of FOC, to realize the torque command using (4.2). It transforms the stator currents into *d* and *q* components aligned with the rotor flux position θ_m.

1. Current References:
    - ○ i_{sq}^*: Calculated from the torque reference: $i_{sq}^* = \frac{2T_e^*}{3N_p\psi_f}$. (4.2)
    - ○ I_{sd}^*: Set to 0 (Zero D-Axis Current control). This minimizes resistive losses as all current contributes to torque.
2. Current Controllers: Two PI controllers regulate the error between measured and reference currents ($i_{sd}^* - i_{sd}$ and $i_{sq}^* - i_{sq}$).
3. Decoupling: Feed-forward terms ($\omega_e L_q i_{sq}$ and $\omega_e L_d i_{sd}$) are added to the PI outputs to cancel the cross-coupling voltage terms (from 3.13 and, 3.14), ensuring independent control of d and q axes.
4. SVPWM: The output voltage references V_{sd}^*, V_{sq}^* are converted to switching signals using Space Vector Pulse Width Modulation (SVPWM) for better DC bus utilization compared to SPWM.

4.3 PITCH ANGLE CONTROL MECHANISM [11]

The pitch controller is a safety mechanism and Fig. 4.3 shows block diagram of pitch angle controller.

- It is based on the logic that when wind speed $v \leq v_{rated}$ (12 m/s), pitch $\beta = 0°$ to maximize capture. When $v > v_{rated}$, the generator speed ω_m tends to exceed the rated limit.
- Implementation: A speed feedback loop compares ω_m with ω_{rated}. The error is fed to a PI controller which outputs the pitch angle reference β_{ref}.
- Actuator Model: The physical pitch mechanism has finite speed. It is modelled as a first-

order lag system with rate limiters (±3°/s typically) to simulate hydraulic/electric motor dynamics.

$$\beta = \frac{1}{1+s\tau}\beta_{ref} \tag{4.3}$$

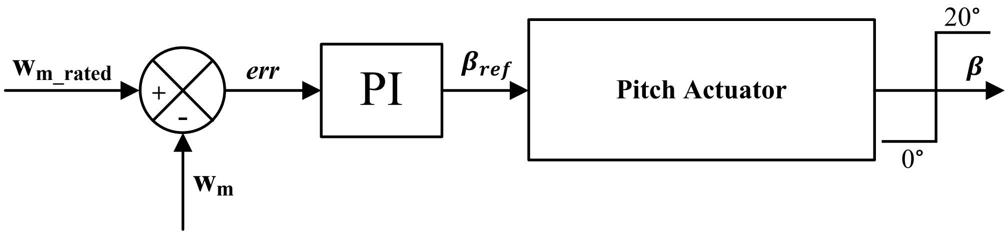

Fig. 4.3. Pitch angle controller block.

4.4 GRID SIDE CONTROL (GSC) STRATEGY UNDER NORMAL CONDITION [12-20]

The VOC is used by the grid side subsystem to regulate the DC-Link voltage. When the grid voltage vector and the synchronized reference frame's d-axis line up, the system is running normally. Consequently, the voltage component on the q-axis is set to zero. The control scheme is shown in Fig. 4.4. Consequently, the power expressions for reactive (Q) and active (P) powers are as follows:

$$P = \frac{3}{2}V_d i_d + V_q i_q \tag{4.4}$$

$$Q = \frac{3}{2}V_q i_d + V_d i_q \tag{4.5}$$

Two cascaded loops make up the GSC control depicted in Fig. 4.4: an inner loop that regulates grid current and an outer loop that controls DC-link voltage (V_{dc}). The following are the inner and outer controller equations:

$$V_d{}^* = R_g i_d + L_{dg}\frac{d}{dt}i_d - w_e L_{qg} i_q \tag{4.6}$$

$$V_q{}^* = R_g i_q + L_{qg}\frac{d}{dt}i_q + w_e L_{dg} i_d \tag{4.7}$$

where R_g. is the grid side line resistance (Ω), L_{dg} and L_{qg} are the inductances (H) of the d and q axes, respectively, w_e is the rotor angular speed (rad/s), i_d and i_q is the grid side current at the d and q axis, respectively.

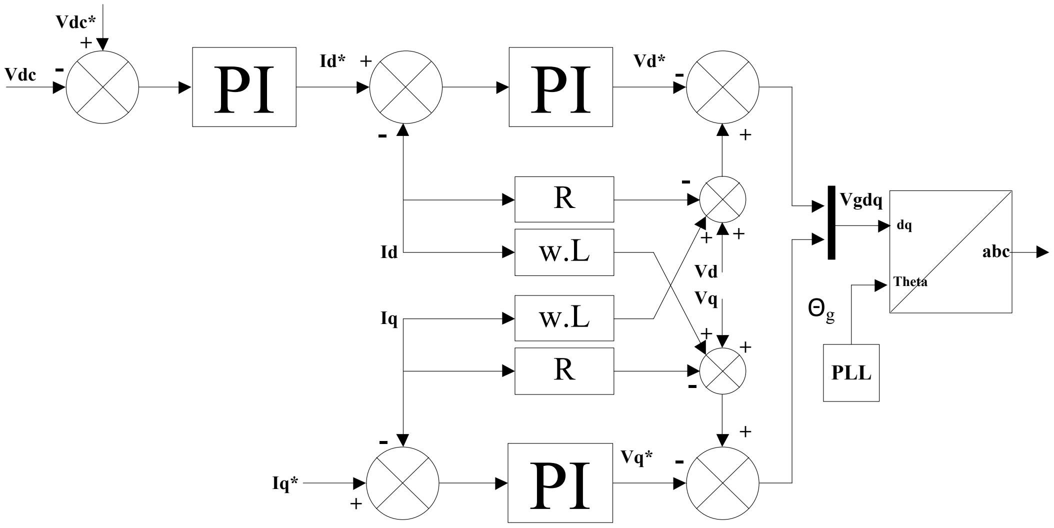

Fig. 4.4. Grid side control scheme.

The GSC controls the voltage at the dc-link and the system's reactive power using voltage-based control. Grid q-axis base current is set to zero, while d-axis base current is generated from the external loop control of V_{dc}. The base i_d^* is obtained by comparing reference V_{dc}^* to the actual value of V_{dc}. The actual d-axis and q-axis currents id and iq, which are measured from the system, were compared to the obtained currents i_d^* and i_q^*. To control id and iq to their appropriate values, two PI controllers must be built and adjusted. Following correction, the Inverse Parks transformation is used to translate the projected d and q axis reference voltages (V_d^* and V_q^*) into an ABC frame.

4.5 GRID SIDE CONTROL (GSC) STRATEGY UNDER ABNORMAL CONDITION [20-25]

During abnormal grid conditions, such as asymmetrical or symmetrical short-circuit faults, the utility grid experiences sudden and severe voltage sags. Under these transient states, the primary objective of the GSC is to shifts its focus from maximum active power export to grid stabilization and self-protection. The control scheme should rapidly adapt to prevent the DC-link voltage from reaching hazardous levels while simultaneously managing the grid currents to comply with statutory fault ride-through requirements.

4.5.1 GSC Conventional Grid Codes and LVRT under Abnormal Condition

To prevent cascading grid failures caused by the sudden disconnection of large-scale wind farms, modern transmission operators enforce strict LVRT mandates. Under standard grid codes, such as those defined by the CEA of India, a wind turbine must remain synchronized with the grid during voltage dips and actively inject reactive power to aid in voltage recovery. The GSC functions as an inverter, interfacing the DC link to the AC grid. Fig. 4.5 shows GSC control scheme block diagram.

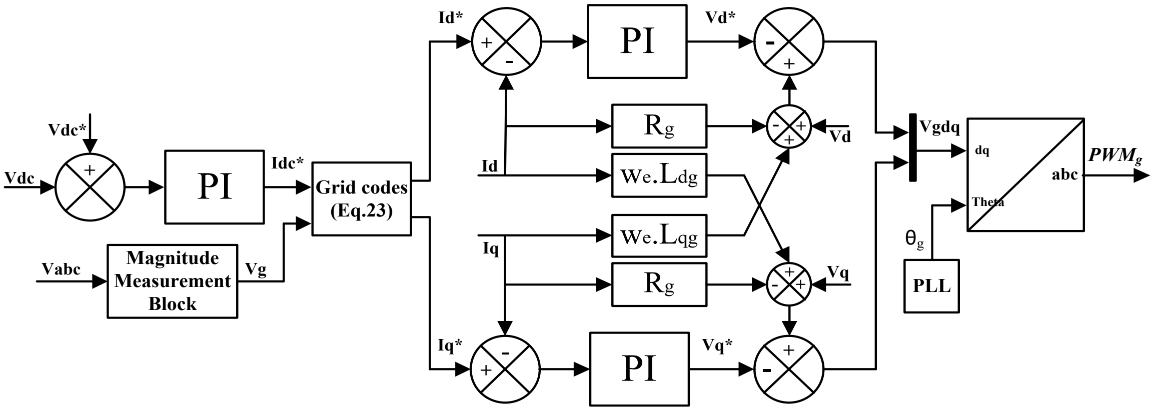

Fig. 4.5. Block diagram representation of GSC conventional method.

The d- and q-axis reference voltages ($V_d{}^*$ and $V_q{}^*$) are converted into the ABC frame using Inverse Park's transformation. Additional blocks, such as the voltage measurement or sag detector block and the grid code implemented as illustrated in (4.8), are also added to the standard GSC controller in Fig. 4.5. Depending on the depth of voltage sag, these grid codes specify the system performance under LVRT conditions that need the decrease of I_d^* and the increase of I_q^*.

$$\begin{cases} \begin{cases} I_d^* = I_{dc}^* \\ I_q^* = 0 \end{cases} & if\ \ 0.9V_n \le V_g \le V_n \\ \begin{cases} I_d^* = \sqrt{(I_n)^2 - \left(I_q^*\right)^2} \\ I_q^* = 2\left(1 - V_g/V_n\right)I_n \end{cases} & if\ 0.5V_n \le V_g \le 0.9V_n \\ \begin{cases} I_d^* = 0 \\ I_q^* = I_{dc}^* \end{cases} & if\ 0 \le V_g \le 0.5V_n \end{cases} \tag{4.8}$$

According to (4.8), there is no need to inject reactive current if the grid voltage sag is less than 10%. As a result, $\boldsymbol{I_q^*}$ is set to zero. Similarly, there is a corresponding drop in $\boldsymbol{I_d^*}$ and a rise in $\boldsymbol{I_q^*}$ share when voltage sag is between 10% and 50%. Reactive power support is required for extremely severe voltage sag of more than 50%. As a result, active power injection is reduced to zero while $\boldsymbol{I_q^*}$ is maximized. It should be mentioned that GSC control based on the traditional LVRT scheme can only provide a stable system under low to medium voltage sag conditions; it is unable to stabilize the system under high sag conditions. In order to automatically identify voltage sag and calculate the necessary reactive power supply under various sag scenarios, an ANN architecture has been trained and modelled.

4.5.2 GSC LVRT Enhanced Control Using ANN Technique

The ANN is trained to continuously monitor real-time grid state variables (such as Point of Interconnection (POI) voltage and DC-link variations) and instantly predict the optimal active and reactive current references (i_d^* and i_q^*) required to stabilize the system. However, because PI controllers are linearly tuned for specific, nominal operating points, their transient response is inherently sluggish during deep, non-linear grid faults. During a grid fault, the ANN bypasses the sluggish response of the conventional outer voltage loop. It immediately commands the exact reactive current necessary to satisfy grid code requirements while actively modulating the active power flow to strictly regulate the DC-link voltage.

Artificial Neural Network (ANN) Architecture: [22-25]

27

A Two-Layer Feedforward Neural Network, as depicted in Fig. 4.6, is the network design utilized for this assignment. An input layer, one hidden layer, and an output layer make up the network's three layers.

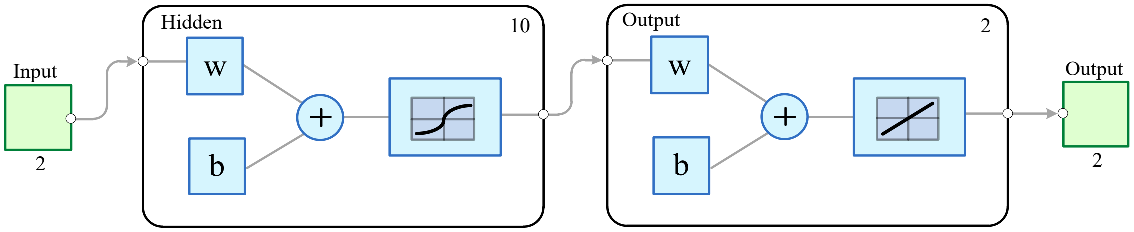

Fig.4.6. Block diagram representation of ANN architecture used for LVRT.

25

The grid voltage magnitude (V_g) in pu and the active current reference from the DC link controller (I_{dc}^*) are the two inputs that the ANN input layer takes into account. For optimal performance, a hidden layer with ten neurons uses the tansig function to understand the intricate, nonlinear interactions between the inputs and outputs. The output layer has two neurons that correspond to the goal outputs: the final d-axis current reference (I_d^*) and the q-axis current reference (I_q^*). The linear or purelin transfer function is employed in this layer.

Next, the ANN's training is covered.

Levenberg-Marquardt (LM) Training Algorithm

The neural network is trained using the least squares method via the LM algorithm, a high-performance optimization tool. Equation (4.9) provides the rule for the network's weights (w) in the LM algorithm:

$$\Delta w = -(J^T J + \mu I)^{-1} J^T e \tag{4.9}$$

where I is the identity matrix, μ is the damping parameter, e is the error vector, and J is the Jacobian matrix, which contains the first-order partial derivatives of the network errors with respect to each weight.

Fig. 4.7 shows the model of GSC integrated with ANN block. ANN block has two inputs; V_g in per-unit and $I_{dc}{}^*$ and has two outputs; $I_d{}^*$ and the $I_q{}^*$. The ANN weights are updated using LM technique discussed above. Fig. 4.8 shows the results of the trained ANN in form of mean square error and regression plots.

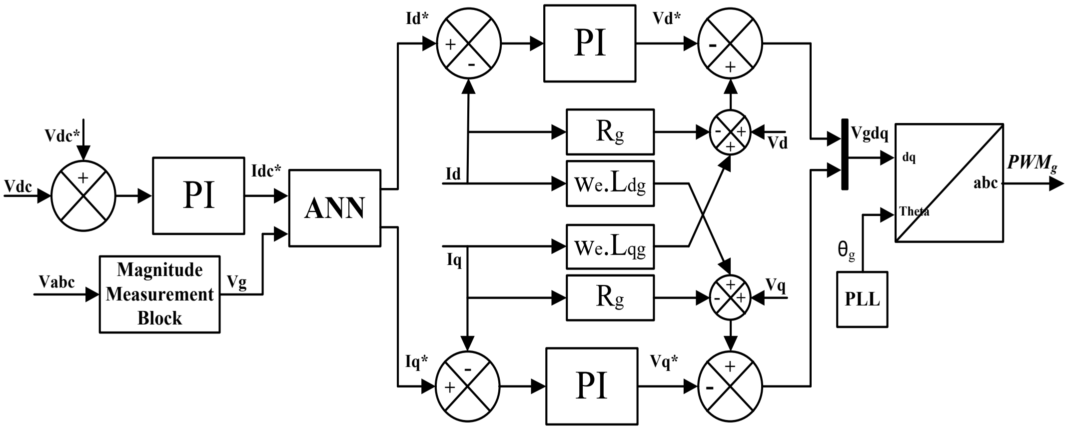

Fig. 4.7. Block diagram of GSC with integrated ANN.

The results of training, validation, and test errors are presented as a function of training epochs in Figure 4.8 (a). Plotting the Mean Squared Error (MSE) reveals that the highest validation performance is reached at epoch 221, which corresponds to a minimal MSE of 7.755×10–^{8}. The associations between the ANN outputs and the training, validation, testing, and total dataset targets are displayed in the regression plots.

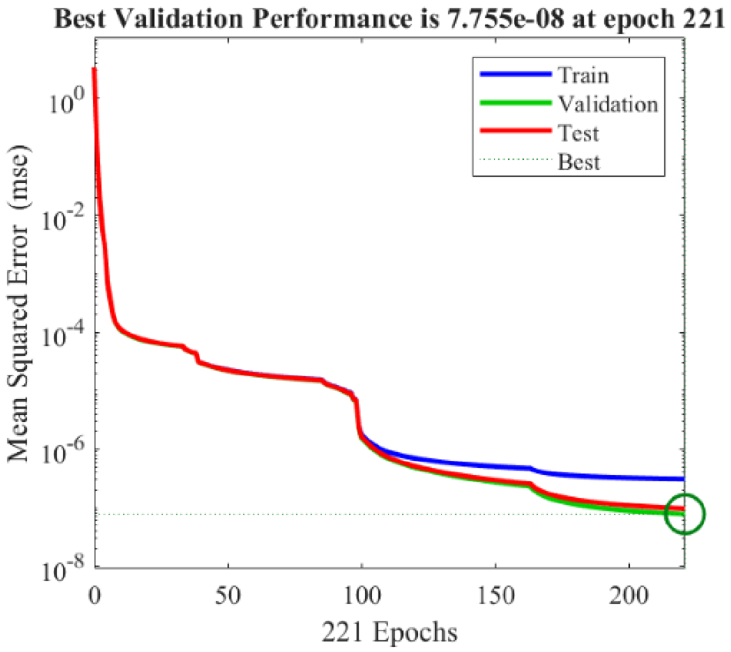

(a) Mean squared error plot

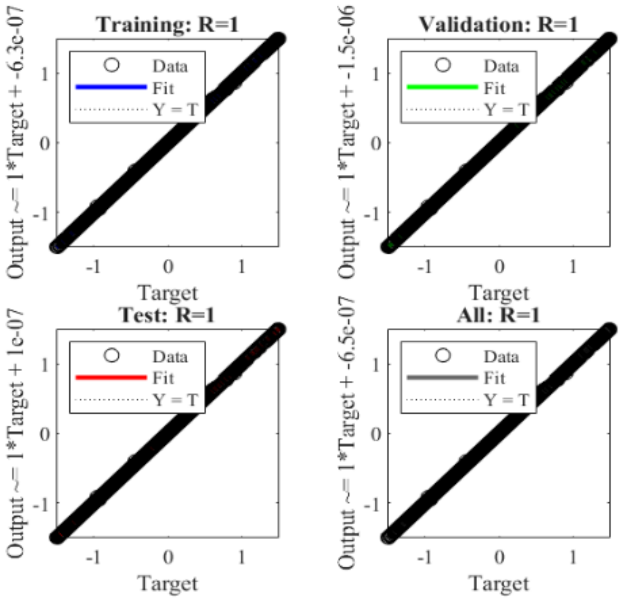

(b) Regression plot

Fig. 4.8. ANN training results, (a) mean squared error plot, and (b) regression plot

The correlation coefficient R=1 in every instance indicates a perfect linear relationship, meaning that the ANN outputs almost precisely match the targets. This demonstrates that the ANN network is well-trained and accurately and robustly approximates the nonlinear mapping required for enhanced LVRT control.

4.6 Cyber Attack Vector Formulation [26-39]

To rigorously evaluate the system's cyber-physical vulnerabilities, this section outlines the mathematical formulation and simulation methodology used to inject FDI, DoS, Replay, and Control Parameter attacks into the converter control loops. By explicitly defining these attack vectors, it establishes the operational framework for assessing the dynamic impact of malicious data manipulation on the wind turbine's stability

4.6.1 Attack Using False Data Injection (FDI) [36]

By inserting malicious data $\alpha(t)$into a sensor feedback loop, an FDI attack jeopardizes system integrity. The controller receives y_m, the compromised measurement:

$$y_m(t) = y_{true}(t) + \alpha(t) \tag{4.5}$$

One important stability variable focused in this work is the DC link voltage sensor. A step function $\alpha(t)$ applied to the V_{dc} signal is used to model the attack.

4.6.2 Denial-of-Service (DoS) Attack [37]

The goal of a denial-of-service attack is to render a resource inaccessible. This attack is simulated by a packet loss or communication jam on the GSC's PWM command channel. At the moment of attack, t_a , the converter-side command, PWM_g, is nullified:

$$PWM_g(t) = \begin{cases} PWM_g(t), t < t_a \\ 0, \qquad\quad t \geq t_a \end{cases} \tag{4.6}$$

4.6.3 Replay Attack [38]

In a replay attack, an adversary secretly records a portion of valid sensor data and plays it back to the controller later, τ .

$$y_m(t) = y_{true}(t - \tau) \tag{4.7}$$

To test the system's reaction to a physical fault as voltage sag. This sag condition arises during the replay attack is initiated.

4.6.4 Control Parameter Attack [39]

The assumption behind this intrusive attack is that the attacker has access to the controller memory and is able to change its settings. This attack is simulated as an attack on the PI gains of the V_{dc} regulator, transforming them from their tuned, stable values (K_p^{dc}, K_i^{dc}) to malicious values ($K_{p,mal}^{dc}$, $K_{I,mal}^{dc}$) at t_a.

4.7 SIMULINK MODEL

The complete grid-connected PMSG wind energy conversion system gets modelled and simulated in MATLAB/Simulink to evaluate it under dynamic conditions. Fig. 3.4 depicts the consolidated system diagram, the diagram brings together the physical electric plant and layers of advanced, hierarchical control subsystems.

The physical power circuit comprises a 575 V AC utility grid, an RL (inductive-resistive) grid filter, a B2B full-scale converter, and PMSG. This back-to-back converter has two parts, MSC and GSC, with a central DC-link capacitor sitting in between. Table 4.1 gave the overall summary for the equations used to designing MSC and GSC control logic.

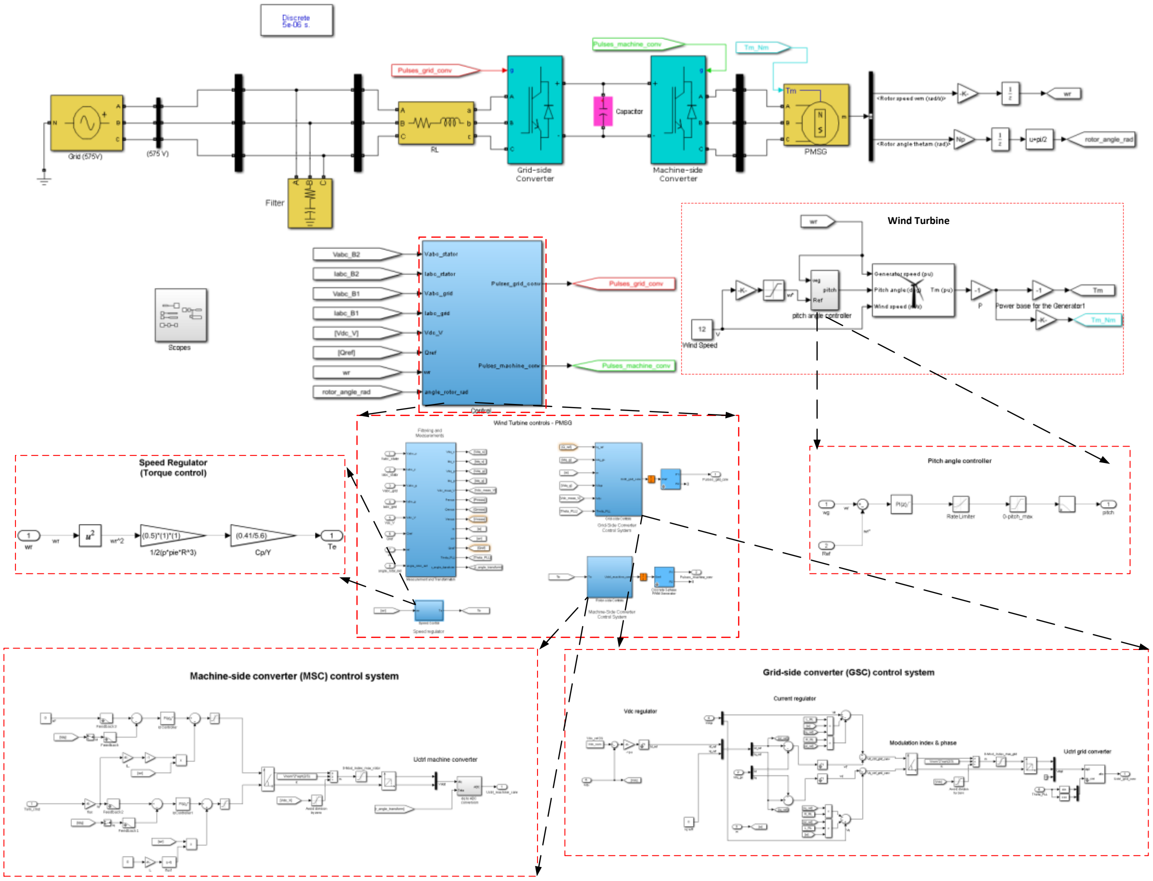

Fig. 3.4. PMSG-based WECS MATLAB/Simulink diagram.

TABLE 4.1: SUMMARY OF MATHEMATICAL EQUATIONS FOR MSC AND GSC COMPONENTS

System Component	Parameter Modelled	Governing Equation
Machine Side Control	Electromagnetic Torque (T_e)	$T_e = \frac{1}{2}\rho A C_p(\lambda,\beta)\left(\frac{w_m R}{\lambda}\right)^3 \Big/ w_m$
	Stator d-axis Voltage ($\mathrm{V_{sd}}$)	$\mathrm{V_{sd}} = \mathrm{R_s i_{sd}} + \frac{\mathrm{d\psi_{sd}}}{\mathrm{dt}} - \omega_\mathrm{e}\psi_\mathrm{sq}$
	Stator q-axis Voltage ($\mathrm{V_{sq}}$)	$\mathrm{V_{sq}} = \mathrm{R_s i_{sq}} + \frac{\mathrm{d\psi_{sq}}}{\mathrm{dt}} + \omega_\mathrm{e}\psi_\mathrm{sd}$
Grid-Side Converter	Grid d-axis Voltage (V_d)	$V_d{}^* = R_g i_d + L_{dg}\frac{d}{dt}i_d - w_e L_{qg} i_q$
	Grid q-axis Voltage (V_q)	$V_q{}^* = R_g i_q + L_{qg}\frac{d}{dt}i_q + w_e L_{dg} i_d$
	Active Power (P)	$P = \frac{3}{2}V_d i_d + V_q i_q$
	Reactive Power (Q)	$Q = \frac{3}{2}V_q i_d + V_d i_q$

4.7 CONCLUSION

This chapter presented a comprehensive control schemes designed for the grid-connected PMSG wind energy conversion system in different operating modes. Initially, the modelling confirmed that under normal grid conditions, the MSC and GSC effectively executed MPPT and stable active power export, respectively, while maintaining nominal DC-link voltage.

However, the analysis of abnormal conditions highlighted significant limitations in the conventional control architecture. While the standard PI based controllers could only handle minor voltage sags and false to provide LVRT support under severe faults. That problem gets fixed by the use of an ANN based LVRT controller. ANN controller boosts the system's response under stress, stopped the DC-link voltage from shooting up drastically and enhance the wind turbine's LVRT capability.

Finally, this chapter discussed modelling of various cyber-attacks like FDI, DoS, Replay and control Parameter attacks.

CHAPTER 5

RESULTS and SIMULATION

5.1 SIMULATION SETUP

The proposed 4 MW PMSG WECS was simulated using MATLAB/Simulink 2024a. The parameters were selected to represent a typical commercial multi-megawatt turbine. The results section has been divided into three cases viz. under normal grid conditions (Case I), Conventional Grid Code-Based Approach (Case II) and Enhanced ANN based LVRT technique (Case III).

5.2 CASE I: PERFORMANCE ANALYSIS UNDER VARIABLE WIND SPEED

To validate the transient response, a variable wind speed profile was applied.

- Step Response: The wind speed was initialized at 11.5 m/s, dropped to 9 m/s at t=1s, increased to 10 m/s at t=2.9s, and finally stepped to the rated speed of 12 m/s at t=4.2s, as shown in Fig. 5.1 (a).

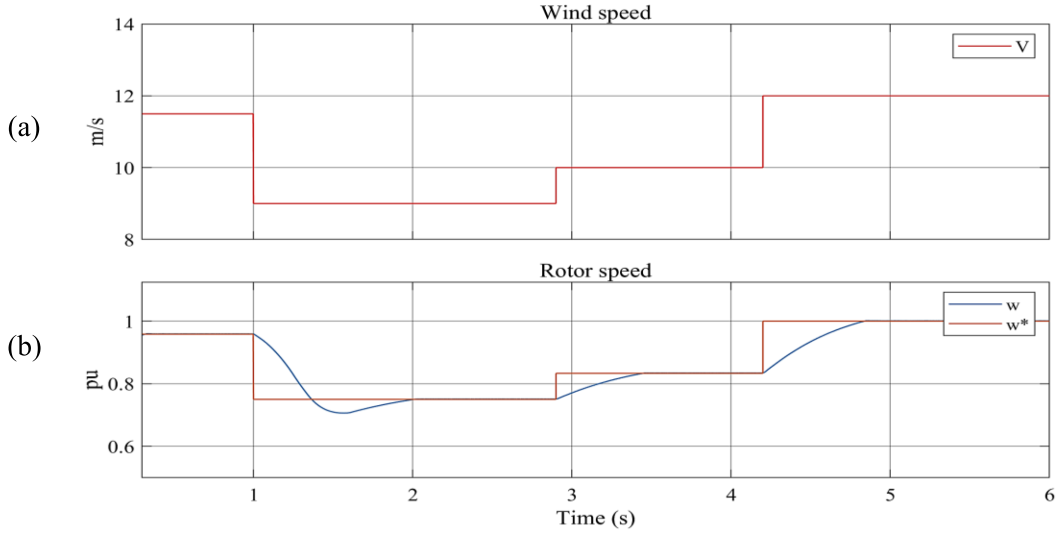

Fig. 5.1. (a) Wind speed, (b) angular Rotor speed in p.u.

- Generator Speed: The rotor speed ω_m tracked the wind speed variations accurately as seen in Fig. 5.1 (b). At 12 m/s, the rotor speed stabilized at the rated value (approx. 18-20 rpm mechanical, converted to electrical frequency). The delay in speed response reflects the large inertia (*J*) of the 4 MW turbine, which acts as a natural low-pass filter for turbulence.

Fig. 5.2 shows the (a) Machine side d-axis current, (b) Machine side q-axis current.

- q-axis Current (i_{sq}): The q-axis current, which produces torque, followed the MPPT reference precisely. As wind speed dropped from 11.5 to 9 m/s, i_{sq} decreased to reduce the electrical braking torque, allowing the rotor to slow down and maintain optimal λ.
- d-axis Current (i_{sd}): The d-axis current was successfully maintained at zero ($i_{sd} \approx 0$) throughout the simulation, confirming the effectiveness of the FOC decoupling. This ensures maximum torque per ampere (MTPA) efficiency.

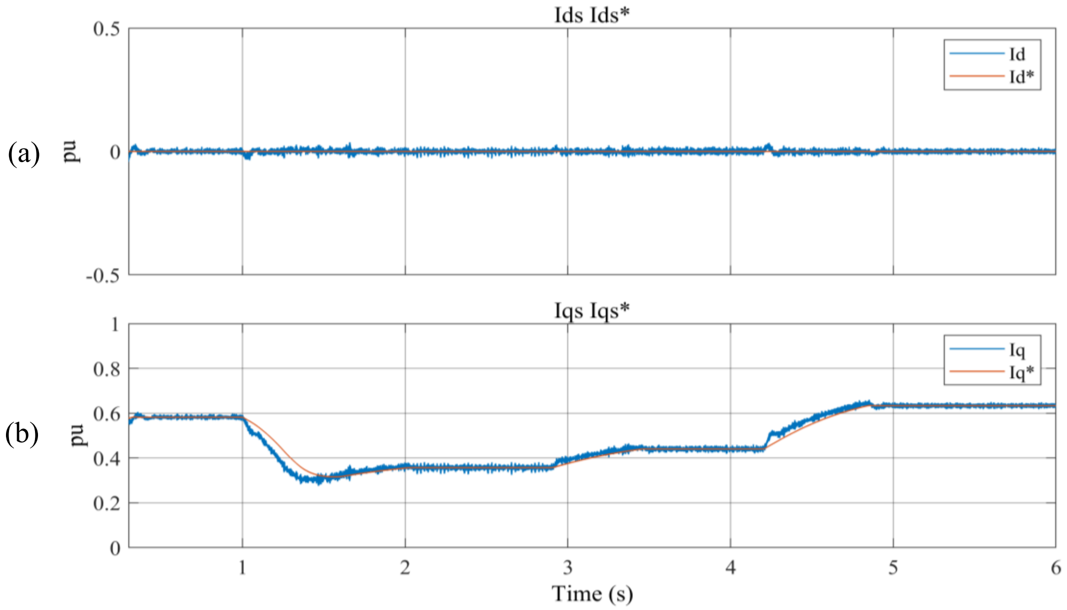

Fig. 5.2. (a) Machine side d-axis current, (b) Machine side q-axis current.

The performance of the Grid Side Converter (GSC) is evaluated by analysing the tracking capability of the d-q axis currents shown in Fig. 5.3. The GSC utilizes a Voltage Oriented Control (VOC) scheme. The following observations are drawn from the simulation results:

- Active Current Tracking (i_d): Fig. 5.3 (b) illustrates the direct-axis grid current (i_d) and its reference (i_d^*). The d-axis current is responsible for active power transfer to the grid.

- Accurate Tracking: The measured i_d (red trace) tracks the reference i_d^* (blue trace) generated by the DC-link voltage controller with high precision, demonstrating the effectiveness of the PI current controllers.
- Power Flow Direction: The negative magnitude of the d-axis current indicates that active power is flowing from the DC link into the grid (inverter mode), which is the desired operation for a wind energy generation system.

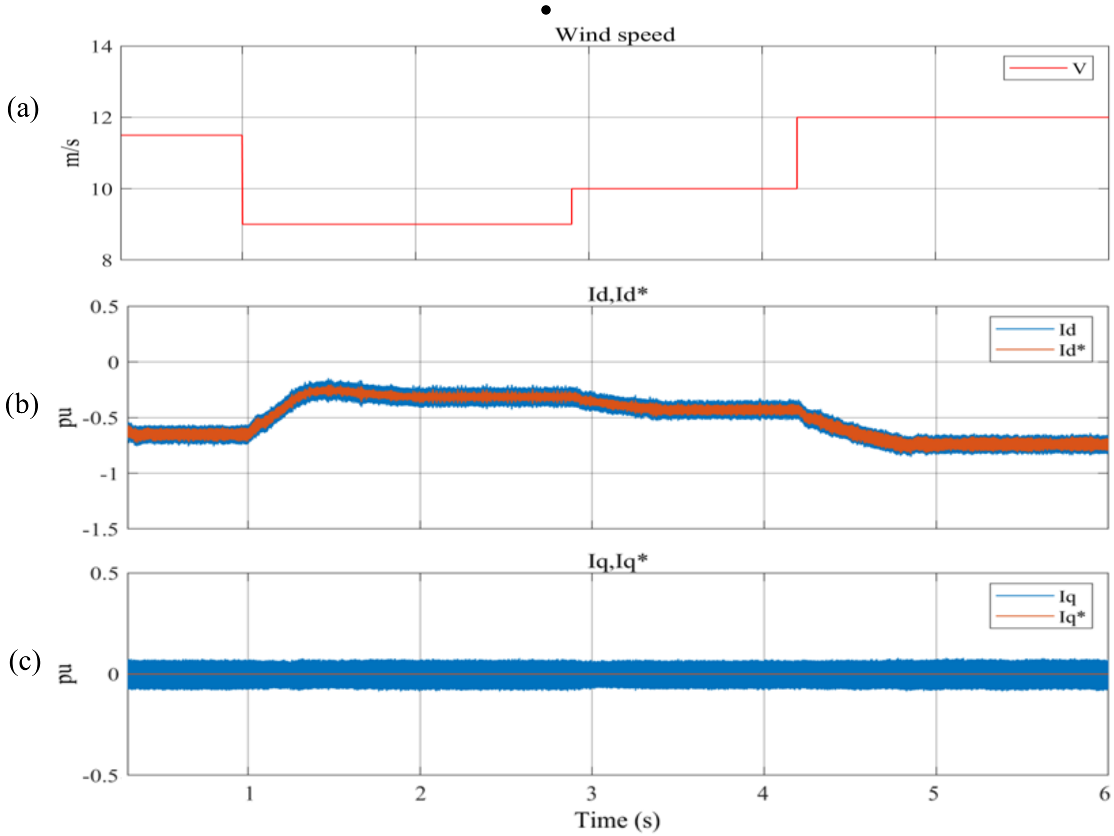

Fig. 5.3. (a) Wind speed, (b) Grid side d-axis current, (c). Grid side q-axis current.,

- Response to Wind Variations: The magnitude of i_d varies dynamically with the wind speed profile to maintain the power balance at the DC link:
    - Region 1 ($0 < t < 1$ s): At a wind speed of 11.5 m/s, the current settles at approximately -0.8 p.u., indicating high power generation.
    - Region 2 ($1 < t < 2.9$ s): As the wind speed drops to 9 m/s at t=10s, the available mechanical power decreases. The DC-link controller automatically reduces the current magnitude to -0.3 p.u. to prevent DC-link voltage collapse.

  - Region 3 (2.9 < t < 4.2 s): Following the wind speed increase to 10 m/s, the current magnitude steps up to approximately -0.6 p.u.
  - Region 4 (t > 4.2 s): When the wind speed reaches the rated 12 m/s, the system extracts maximum power, and the d-axis current reaches its rated value of approximately -1.0 p.u.
- Reactive Current Control (i_q): Fig. 5.3 (c) depicts the q-axis grid current (i_q).
  - Decoupling Effectiveness: The measured $i_q$remains tightly regulated at zero, even during the large step changes in the active current (i_d) at t=1s and t=4.2s. This confirms the operative balance between the d-axis and q-axis control loops, ensuring that floaties in the active power do not disturb the reactive power regulation.
- Transient Response: The system exhibits a fast transient response with negligible overshoot during step changes in wind speed. The settling time is minimal (< 0.5s), indicating that the GSC control parameters are well-tuned for the dynamic operating conditions of the 4 MW wind turbine.

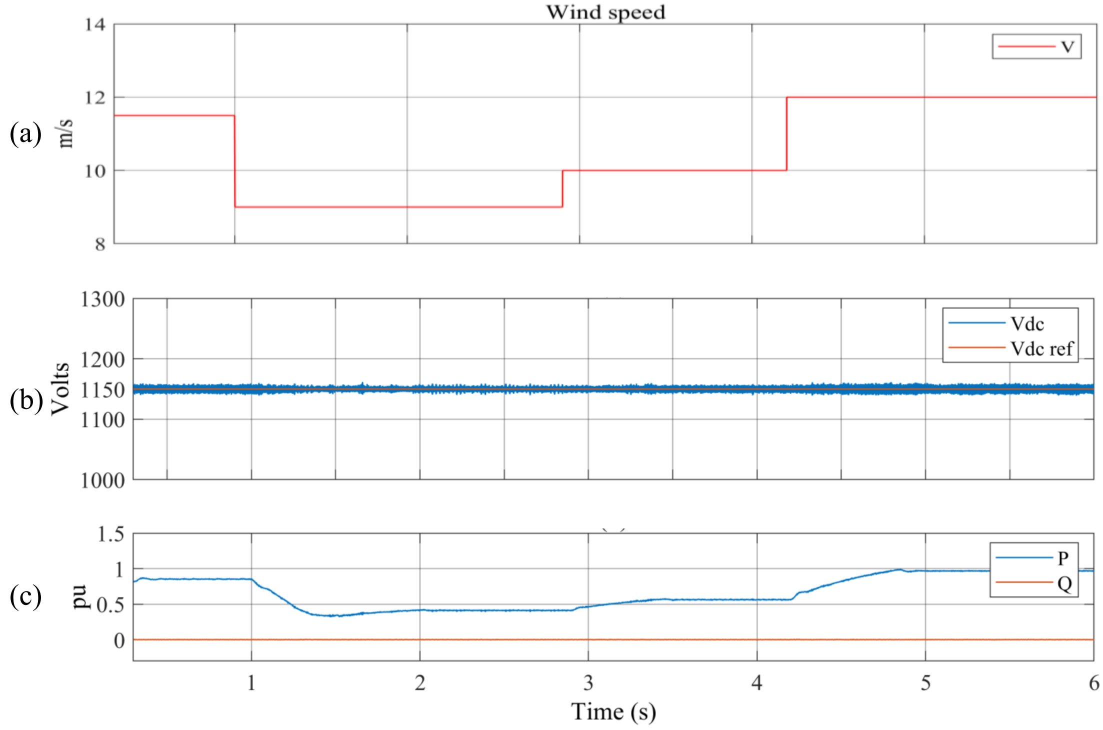

Fig. 5.4. (a) Wind speed, (b) DC-Link voltage.

The DC link voltage is a critical indicator of power balance and Fig. 5.4(b) shows the DC-Link voltage under variable wind speed.

- Regulation: The voltage was regulated at the reference value of 1150 V.
- Transient Response: During the sudden drop in wind speed at t=1s, a small transient dip in V_{dc} was observed. This occurs because the power coming from the generator drops instantly, while the grid inverter takes a few milliseconds to adjust its power export. The PI controller in the VOC outer loop quickly corrected this, restoring 1150 V within acceptable settling times (< 0.5s). This stability proves the robustness of the back-to-back converter control.

The Active and Reactive Power Export is shown in Fig.5.4(c). The reactive power (Q) is strictly maintained at 0 p.u. throughout the simulation, confirming that the GSC successfully operates at a unity power factor without drawing or injecting unnecessary reactive current during normal operation. Concurrently, the active power (P) perfectly mirrors the wind speed profile. This demonstrates the MSC's effective execution of MPPT. Notably, when the wind speed reaches the rated 12 m/s at t = 4.2 s, the active power smoothly ramps up to and stabilizes at the maximum rated output of 1 p.u., validating the fundamental control architecture before the introduction of grid faults or cyberattacks.

5.2.4 Experimental Validation of WECS under Varable wind speed

The OPAL-RT real-time simulation platform shown in Fig. 5.5 was used to experimentally validate the results.

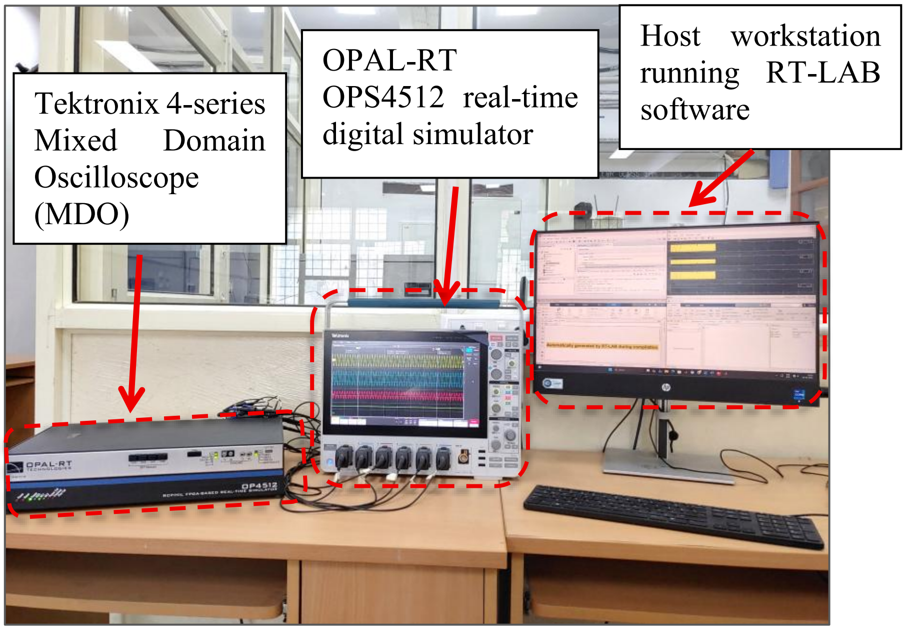

Fig. 5.5 shows the experimental verification setup. The suggested control algorithm is run on the OPAL-RT OP4512 real-time simulator, and a Tektronix 4-series Mixed Oscilloscope is used to record the system reaction through analogy I/O channels.

A high-precision Tektronix oscilloscope was used to track the system outcomes while the control logic was implemented on the OP4512 Field Programmable Gate Array (FPGA)-based simulator. This configuration guarantees that the dynamic performance of the controller satisfies the real-time restrictions necessary for realistic implementations.

Fig. 5.6 shows RT-LAB real-time results for the same system, as the wind speed changes from 10 m/s to 12 m/s.

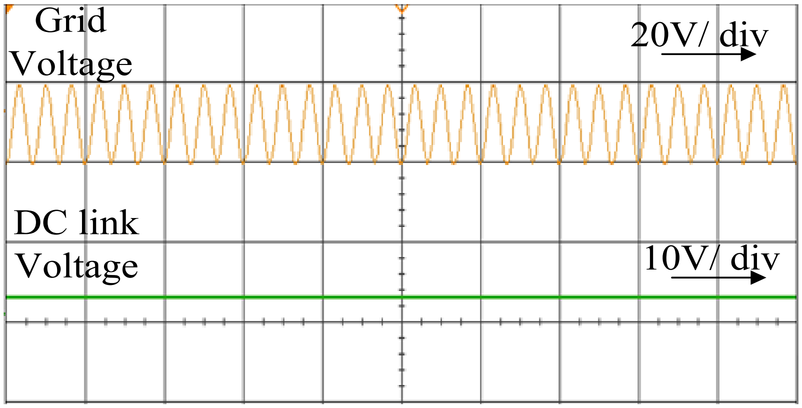

(a) RT-LAB Grid and DC-Link voltage

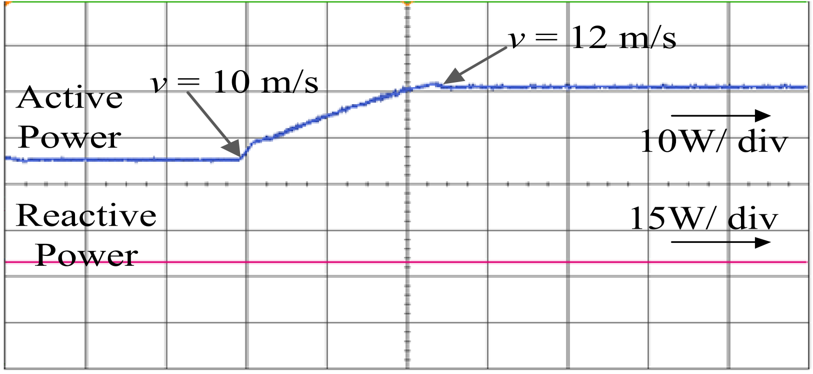

(b) RT-LAB active and reactive power

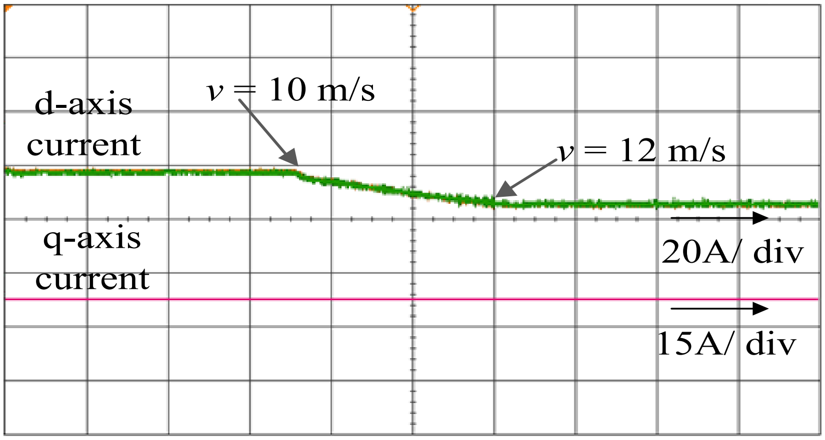

(c) RT-LAB stator-side current

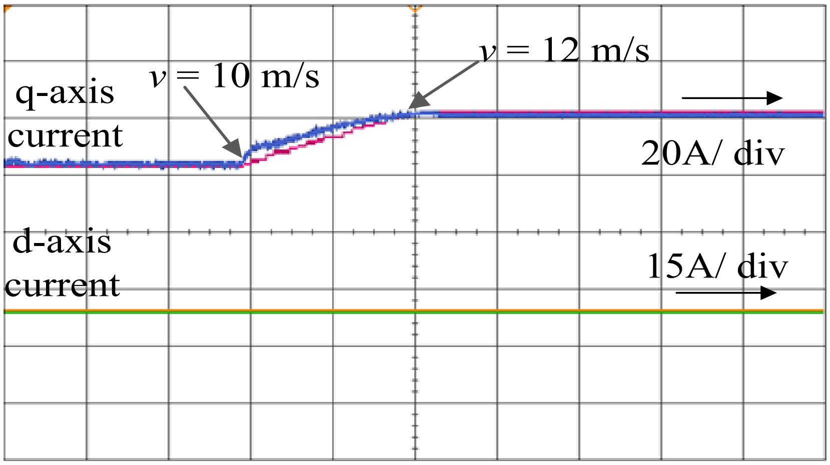

(d) RT-LAB rotor-side current

Fig. 5.6. RT-LAB results under stepped wind speed.

The RT-LAB results in Fig. 5.6 (a,b) verify that the DC-link voltage is controlled and that the simulation model closely matches the injected active and reactive power. While the q-axis component of stator current is zero, the actual value of the d-axis stator-side current roughly resembles the reference. In a similar vein, the d-axis current is maintained at zero and the q-axis component of the rotor-side current accurately follows reference. Overall, the simulation and real-time findings verify that the suggested control technique guarantees stable power transfer and grid code compliance under varying wind conditions.

5.3 CASE II: CONVENTIONAL GRID CODE-BASED APPROACH UNDER LOW /MEDIUM SAG

A conventional control method based on grid codes was first developed and tested on Matlab/Simulink, and the the results were validated over OPAL-RT real time simulator. Testd over different voltage sag conditions are cared out starting from 10% to 15%, and then 20% using converntional LVRT control scheme.The results are discussed below.

5.3.1 Performance under 10% Sag Condition

In the first case, voltage sag of the order of 10% is simulated making the overall system voltage dip from 100% to 90%. According to the grid codes in (4.8), a voltage drop of 10% does not require injection of reactive power into the grid.

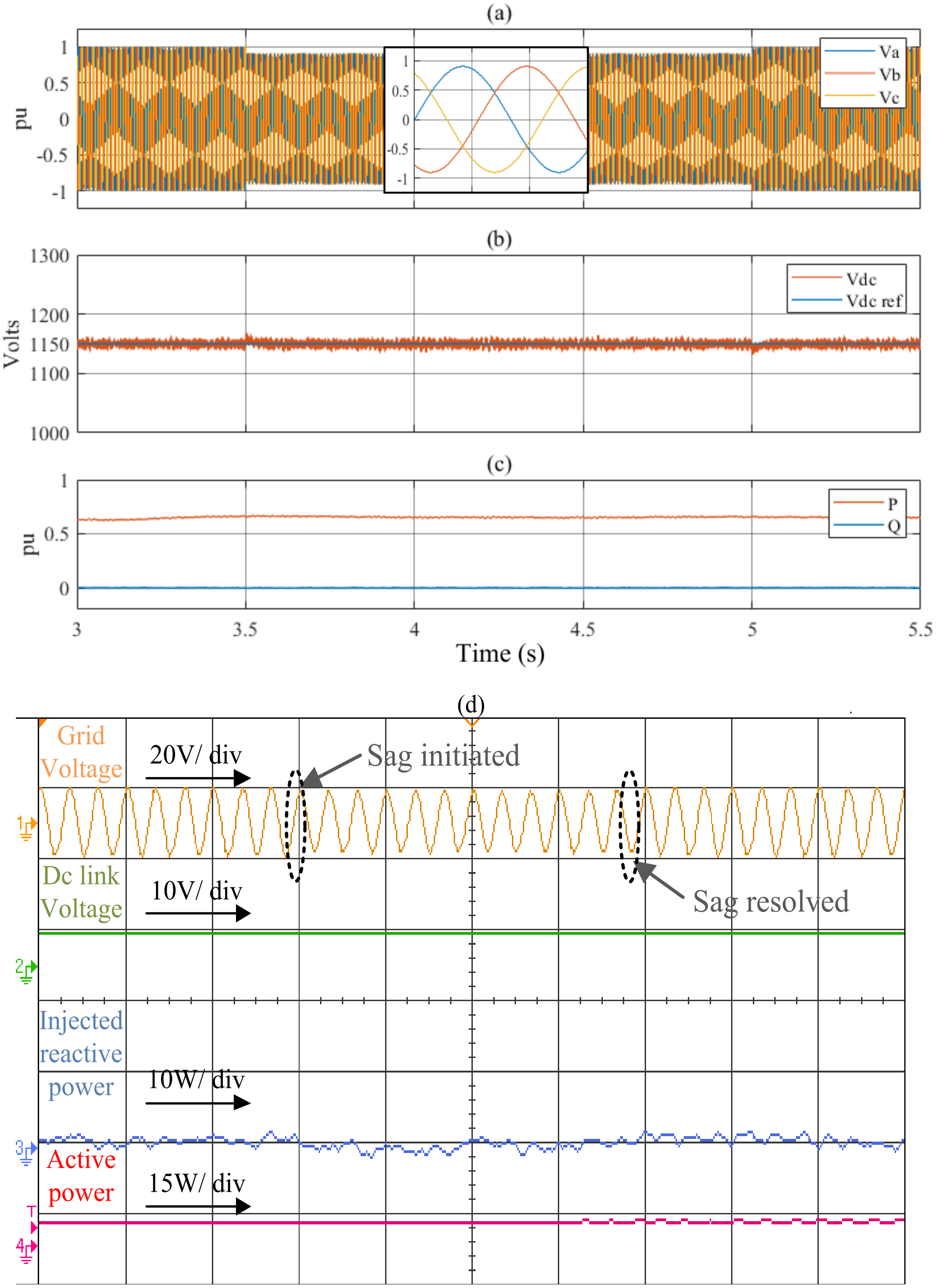

Fig. 5.7. Results using MATLAB/Simulink(a-c) and RT-LAB (d) under 10% voltage sag condition. (a) Grid Voltage (V_{abc}), (b) DC-Link Voltage (V_{dc} and $V_{dc\ ref}$), (c) Power (P and Q), (d) RT-LAB Real-Time Validation.

Fig. 5.7 displays the associated MATLAB/Simulink as well as experimental findings acquired using RT-LAB. The grid voltage Fig. 5.7(a) clearly displays the sag and the recovery that follows. The DC link voltage Fig. 5.7(b) stays near to its reference value, with modest oscillations at the beginning and conclusion of the sag. The stator-side power Fig.

5.7(c) shows that both active and reactive power stay nearly the same since no extra reactive power support is needed during a 10% sag. The RT-LAB validation Fig. 5.7(d) backs up these findings, exhibiting steady grid voltage, controlled DC link voltage, and low fluctuations in active and reactive power during the disturbance.These results show that during moderate voltage sags (≤10%), the system remains stable with traditional grid code–based control. Other test situations under 15% and 20% voltage sag are discused below.

5.3.2 Performance under 15% Sag Condition:

The grid code specified in (4.8) takes effect when the voltage falls to 85%, and in order to keep the grid stable, the necessary reactive power support must be supplied. The grid-side voltage and current waveforms are displayed in Fig. 5.8, and sag is started between 3.5 and 5 seconds. Reactive and active power injection can be seen to vary over the course of the sag. The DC-link voltage, on the other hand, is properly controlled and remains steady at 1150 V prior to, during, and following the sag. The system satisfies the conventional grid code requirements during a 15% sag event, according to the real-time validation findings from RT-LAB hardware.

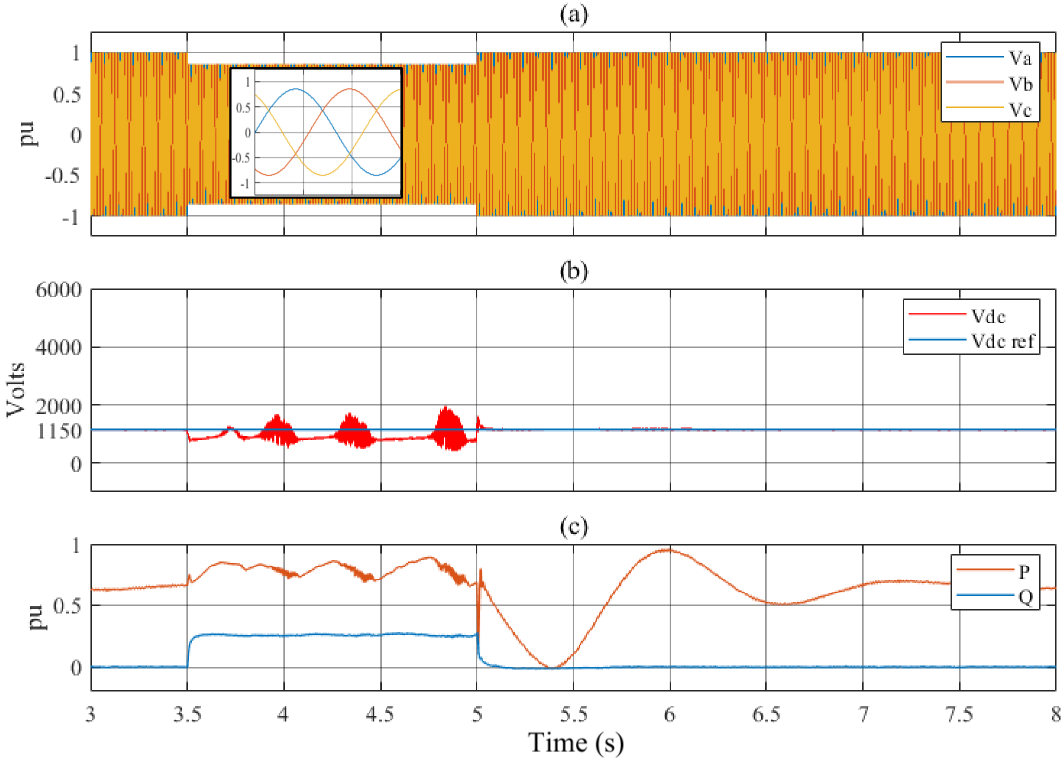

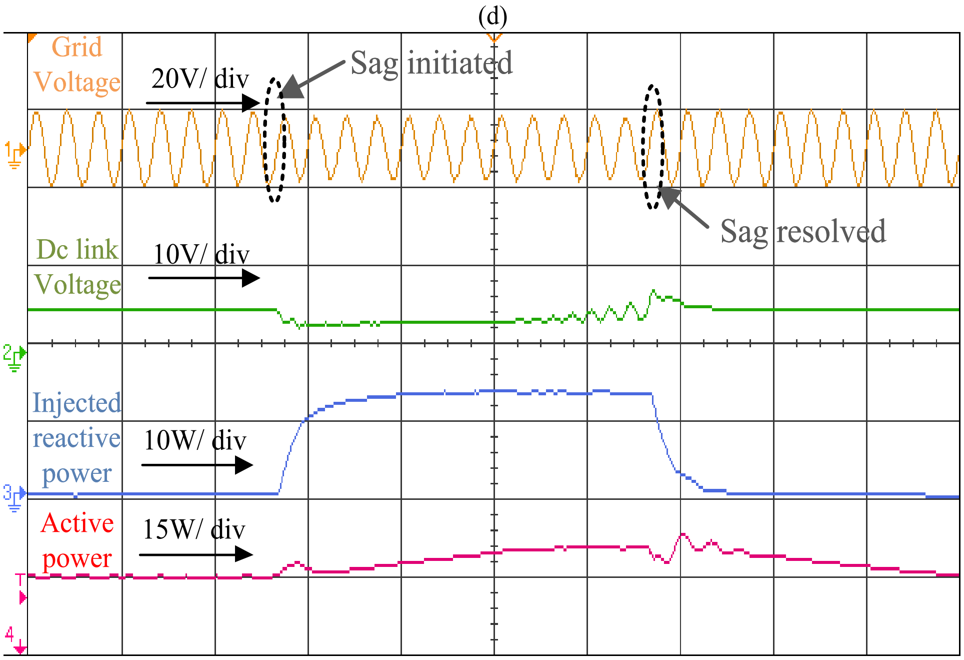

Fig. 5.8. Results using Simulink(a-c) and RT-LAB(d) under 15% voltage sag (a) grid voltage, (b) V_{dc} and $V_{dc\ ref}$, (c) Power (P and Q), (d) RT-LAB Real-Time Validation.

5.3.3 Performance under 20% Sag Condition:

The system experiences a more severe disruption than in the previous situations when the grid-side voltage falls by 20%. For the grid code to remain stable and prevent disconnection, a significant amount of reactive power is needed.

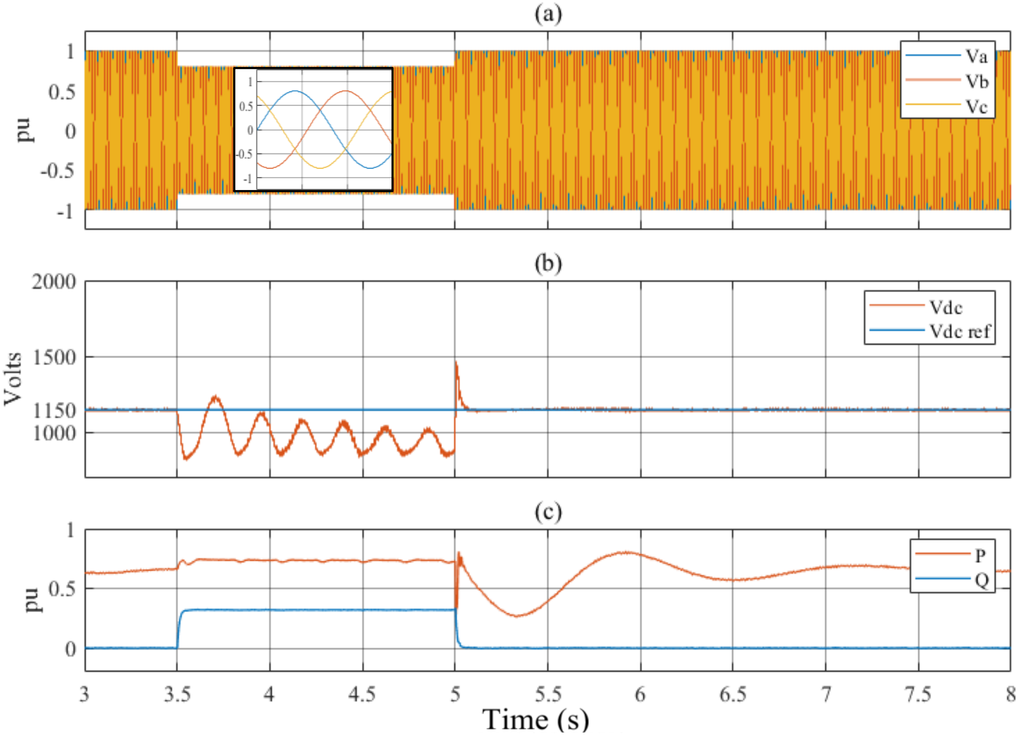

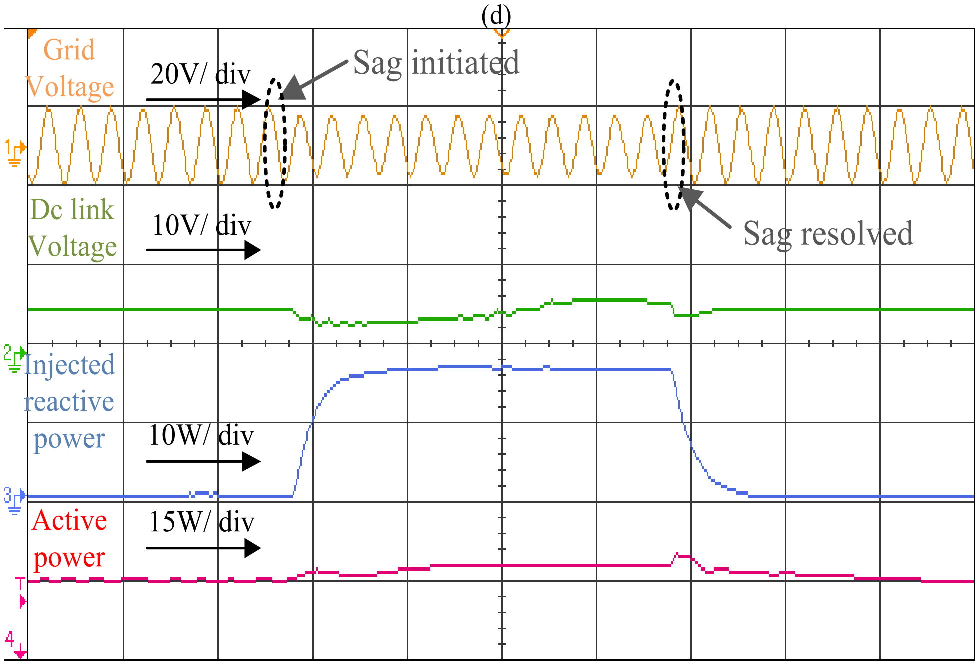

Fig. 5.9. Results under 20% voltage sag conditions. (a) Grid Voltage (V_{abc}), (b) DC-Link Voltage (V_{dc} and $V_{dc\ ref}$), (c) Power (P and Q), (d) RT-LAB Real-Time Validation.

Despite the deeper sag, Fig. 5.9 demonstrates that the DC-link voltage stays constant at its reference value. This attests to the control mechanism's strength. In this scenario, active power fluctuates momentarily before returning to steady-state functioning, but reactive power injection is much higher. With well-controlled DC-link voltage and improved Q support, the real-time RT-LAB implementation supports the theoretical model response shown in Fig. 5.9 (d).

5.4 CASE III: ANN-BASED ENHANCED LVRT TECHNIQUE RESULTS UNDER ABNORMAL CONDITIONS

It can be noted from previous section that the conventional controller performs portly under high voltage sag conditions. Hence, the ANN based LVRT technique is developed and its performance is discussed below.

5.4.1 Performance Under 30% voltage sag condition:

The suggested ANN-based LVRT control was assessed using a 30% grid voltage sag. The grid voltage (Vabc) waveform with a sag of 0.7pu between 3.5s and 5s is displayed in Fig. 5.10(a) the waveform demonstrates complete grid voltage recovery following the fault. This demonstrates that sag detection and adjustment are effective. The DC-link voltage is displayed in Fig. 5.10(b) the DC-link closely resembles its reference. Power (P and Q) is shown in Fig. 5.10(c) active power was maintained at 0.6pu and reactive power at 0.45pu, resulting in a total apparent power of 0.75pu, which is less than the converter's 1.0pu limit. Therefore, there was no need to reduce active power. Fig. 5.10(d) shows RT-LAB Real-Time Validation; hardware-in-the-loop results support the simulation findings. The DC-link voltage remains stable, reactive power is injected during the sag, and active power is maintained.

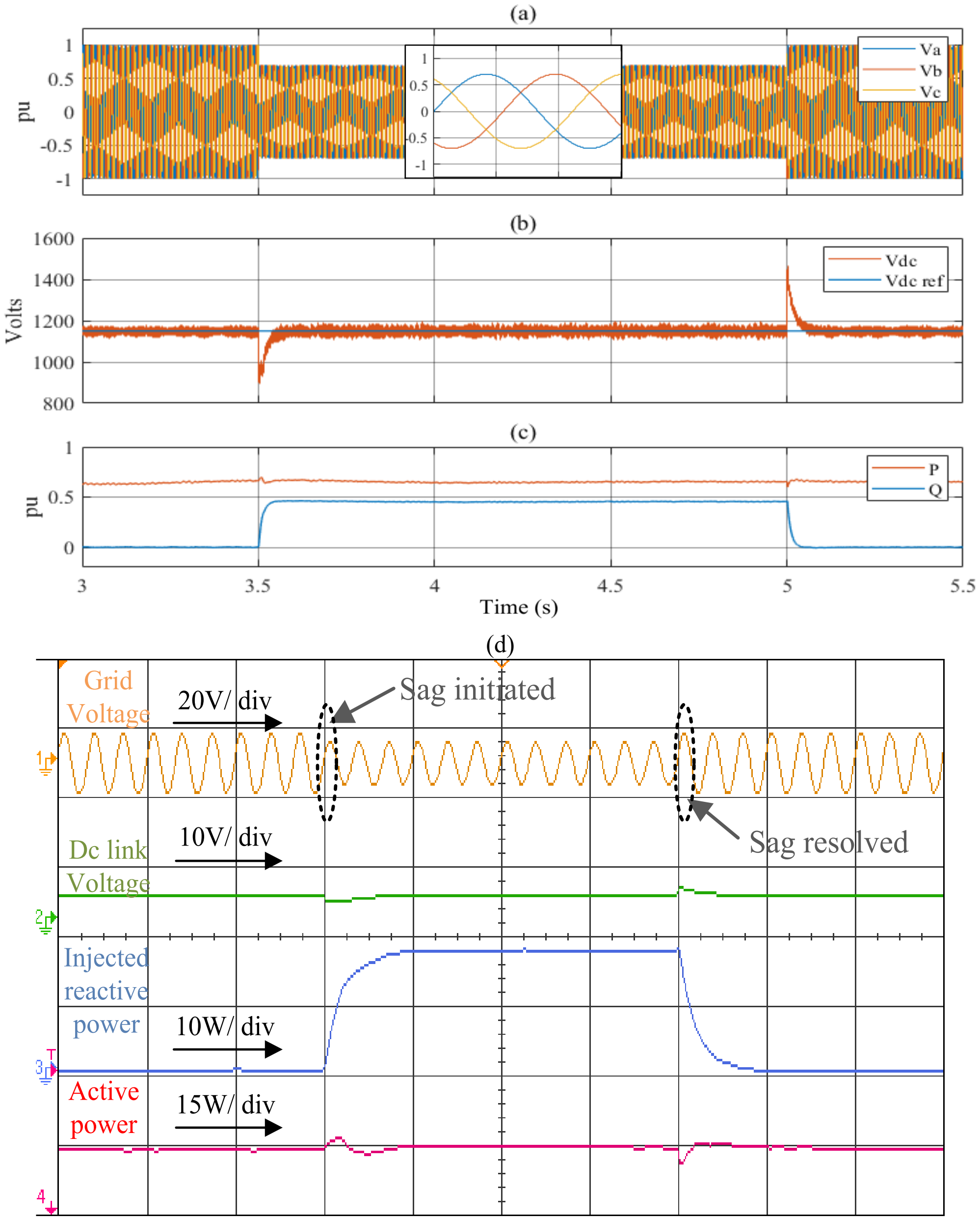

Fig. 5.10. Performance results under 30% voltage sag conditions. (a) Grid Voltage (V_{abc}), (b) V_{dc} and $V_{dc\ ref}$, (c) Power (P and Q), (d) RT-LAB Real-Time Validation.

5.4.2 Performance Under 40% voltage sag condition:

In this case a severe sag of the order of 40% voltage drop is taken to evaluate the performance of the proposed ANN-based LVRT scheme. The conventional controller fails and DC voltage bus regulation cannot be achieved. The results with the ANN controller show the performance in Fig. 5.11 through simulation and experimental results.

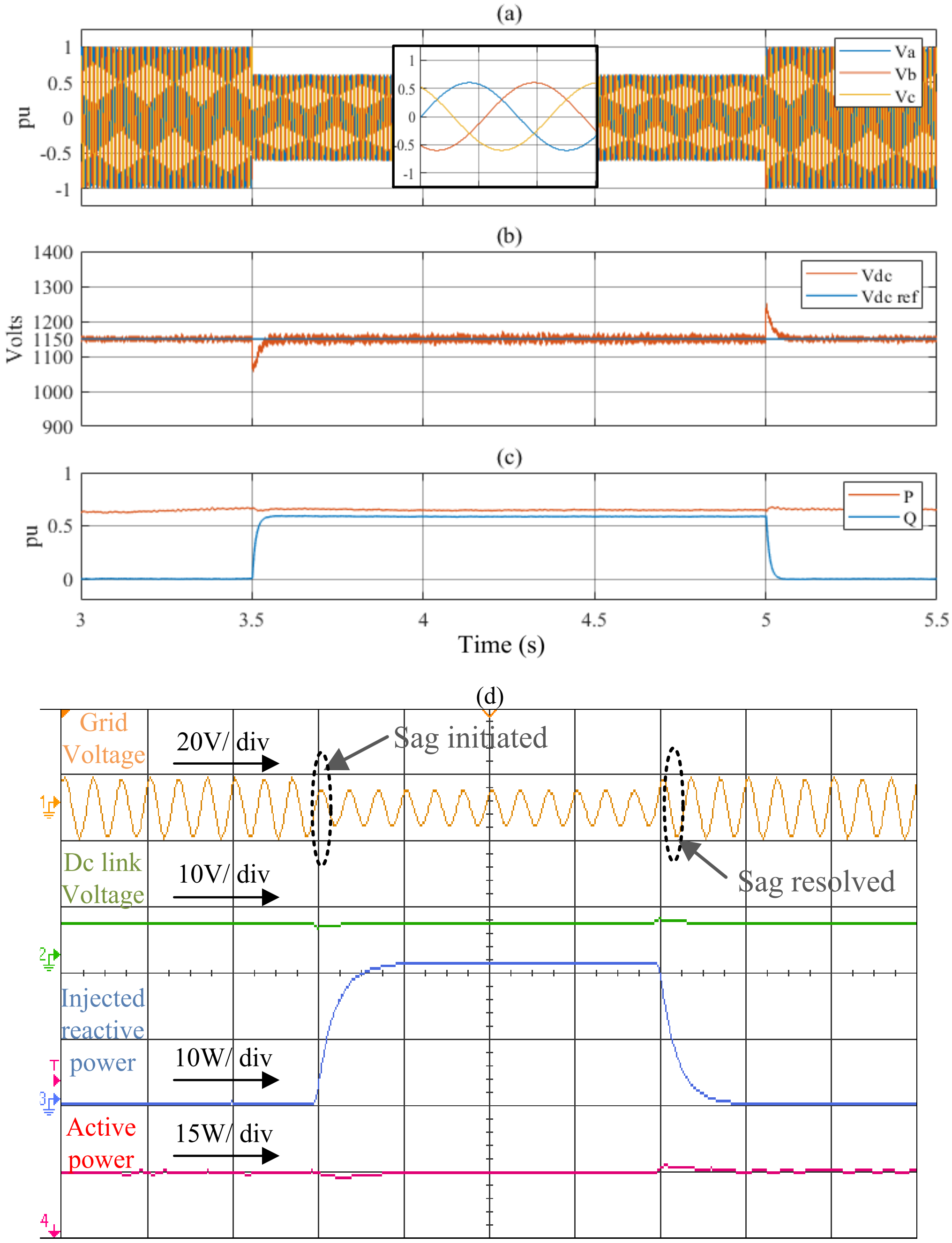

Fig. 5.11. Performance results under 40% voltage sag conditions. (a) Grid Voltage (V_{abc}), V_{dc} and V_{dc_ref}, (c) Power (P and Q), (d) RT-LAB Real-Time Validation.

The grid voltage (V_{abc}) dips to almost 0.6pu during the sag and recovers to nominal once the disturbance is resolved, as shown in Fig. 5.11(a). This indicates that the system is operating properly to be able to identify and mitigate the sag. The DC-link voltage with strong regulation is displayed in Fig. 5.11(b). Power (P and Q) is shown in Fig. 5.11(c); the injected reactive power of 0.55pu increased the total apparent power to 0.8pu within the converter's limitations while the active power remained constant at 0.6pu. Thus, the converter can accommodate both active and reactive power without lowering active power. These results are supported by the RT-LAB real-time validation, as shown in Fig. 5.11(d). The DC link voltage remains constant while the grid voltage clearly shows the sag intervals. While active power supply is unaffected, reactive power injection takes place during the sag. These findings verify that the suggested ANN-based LVRT strategy maintains active power delivery, guarantees DC-link stability, and offers efficient voltage support. In the event of a fault, it also satisfies the grid code criteria.

TABLE 5.1: COMPARISON OF CONVENTIONAL LVRT AND ANN-BASED LVRT METHODS

Cases	Grid Sag Condition	Conventional LVRT	ANN-Based LVRT
Case I	Normal Grid (No Sag)	✓	✓
Case II	Low Sag (10%)	✓	✓
	Low Sag (15%)	✓	✓
	Medium Sag (20%)	✓	✓
Case III	High Sag (30%)	✗	✓
	High Sag (40%)	✗	✓

Table. 5.2 demonstrate that the traditional LVRT approach is effective in low to medium sag circumstances (≤20%), but it is ineffective in severe sag conditions (≥30%). Even high sag levels (30 to 40%) are successfully managed by the ANN-based LVRT strategy, demonstrating its resilience and dependability over the traditional method.

5.5 CYBER ATTACK RESULTS DISCUSSION

The cyberattack is started at $t = 4.5s$, and the simulation runs for 6.5 s for each scenario.

5.5.1 Case 1: FDI Attack on V_{dc} Sensor

A negative step bias of $\alpha = +1400V$ is introduced into the V_{dc} sensor feedback at t = 4.5s. the simulation results are analysed in Fig. 5.12.

The GSC controller detects a false voltage gain., the PI controller saturates, drastically increasing i_d^* to maintain the DC link. The reference DC link voltage (V_{dc}^*) has now changed to 1150 + 1400 = 2550 V. The true V_{dc} starts to increase quickly as reference value changes to 2550 V as observed in Fig. 5.12 (c). As the controller battles the false reading, the system oscillates for the time when fault is simulated. The grid voltage remains unchanged, but the grid current fluctuates at instant of FDI attack.

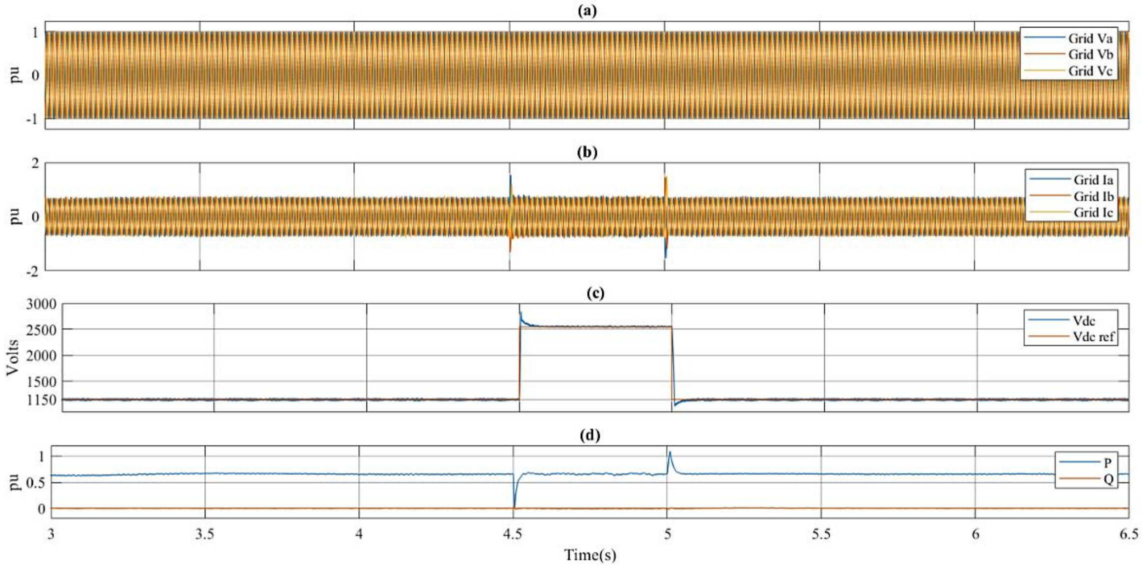

Fig. 5.12. Under FDI attack (a) Grid side Voltage, (b) Grid side Current, (c) DC-link voltage and (d) Grid side active and reactive power.

5.5.2 Case 2: DoS Attack on GSC PWM Commands

In this attack, the adversary jams the communication signals, and this is modelled by setting the pulses of grid side converter signals to zero at t = 4.5s.

The results shows that the GSC switching immediately stops at time= 4.5s. The grid voltage stays unchanged, but the current falls to zero, as shown in Fig. 5.13(a) and Fig. 5.13(b). The system has largely become unstable as evident by a very rapid rise of V_{dc} which can be dangerous. The grid's active power transfer (P) falls to zero as shown in Fig. 5.13(d). The DC link is currently absorbing the entire 4.0 MW from the MSC without an outlet. In milliseconds, the V_{dc} rises up to 18 kV from its reference value of 1.15 kV as shown in Fig. 5.13(c), activating the hardware overvoltage protection and shutting down the turbine completely. This is a severe attack which disables the GSC unit at least temporality from t=

4.5 to 5s till the fault lags, and power transfer (both P, Q) is affected during duration.

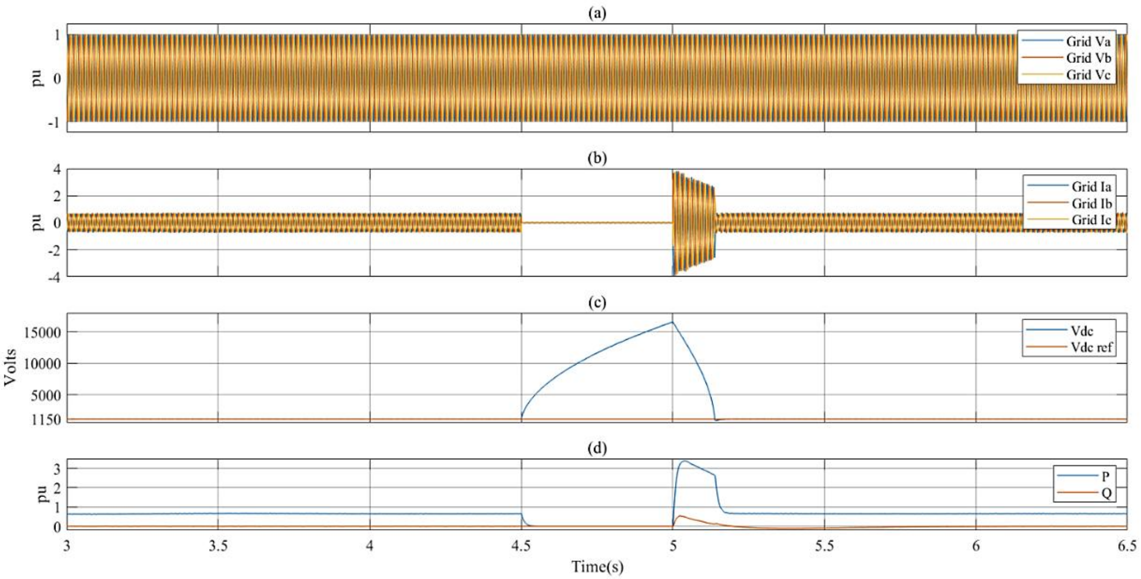

Fig. 5.13. Under DoS attack (a) Grid side voltage, (b) Grid side current, (c) DC-link voltage and (d) Grid side active and reactive power.

5.5.3 Case 3: Replay Attack on $V_{abc,grid}$ Sensors

At t = 4.5s, the replay of pre-recorded "normal" voltage data begins. A three-phase-to-ground fault is applied to the grid at t = 4.51s, resulting in a 70% voltage sag.

The simulation results of this cyberattack are shown in Fig. 5.14. The actual grid voltage collapses and the actual GSC currents ($i_{abc,grid}$) spike to dangerous levels (>2.0 p.u.), as illustrated in Fig. 5.14(b). The replayed "normal" voltage is still being fed into the controller's

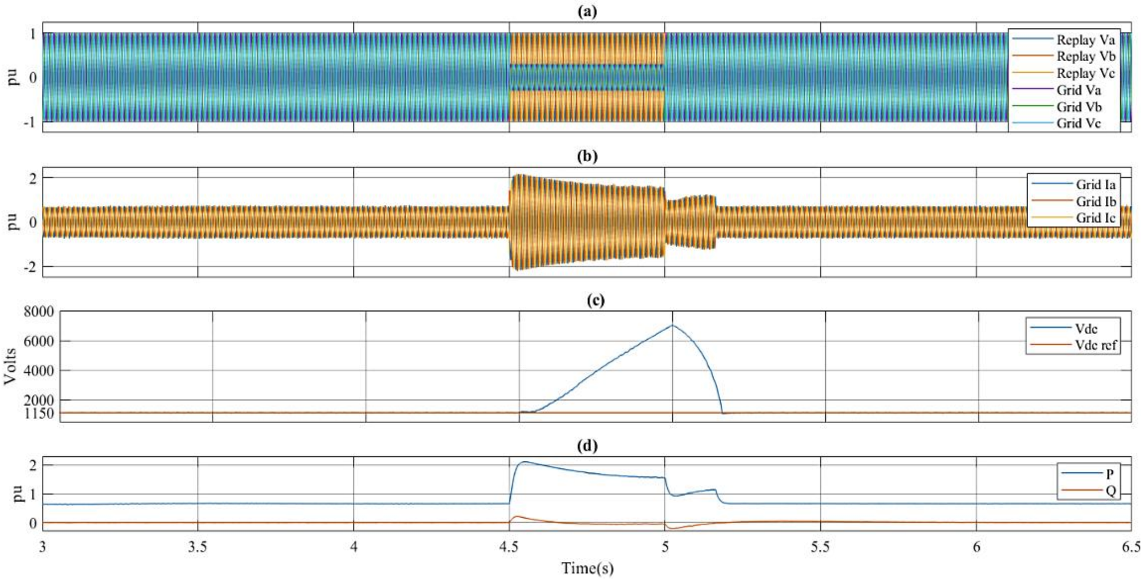

Fig. 5.14. Under Replay attack (a) Grid side voltage, (b) Grid side current, (c) DC-link voltage and (d) Grid side active and reactive power.

PLL and measurement block, as seen in Fig. 5.14(a). The controller is totally unaware of the error.

Importantly, the logic for the system's Low Voltage Ride Through (LVRT) protection, which is intended to identify the sag and modify current commands, does not activate. The V_{dc} rises quickly from reference value of 1.15 kV to 7kV, which is dangerously high, as shown in Fig. 5.14(c). Moreover, a sudden rise and fall of active power (P), with some fluctuations in reactive power are observed as shown in Fig. 5.14(d).

The controller continues to command high current injection into a low-voltage fault, creating a massive overcurrent condition that would physically destroy the converter's IGBTs. This indicates the severity of this Replay Attack.

5.5.4 Case 4: Control Parameter Attack on V_{dc} Regulator

This cyberattack is simulated by changing the V_{dc}regulator's proportional gain $\left(K_p^{dc}\right)$from its stable value of 0.8 to a malicious value of 5.0 at t = 4.5s.

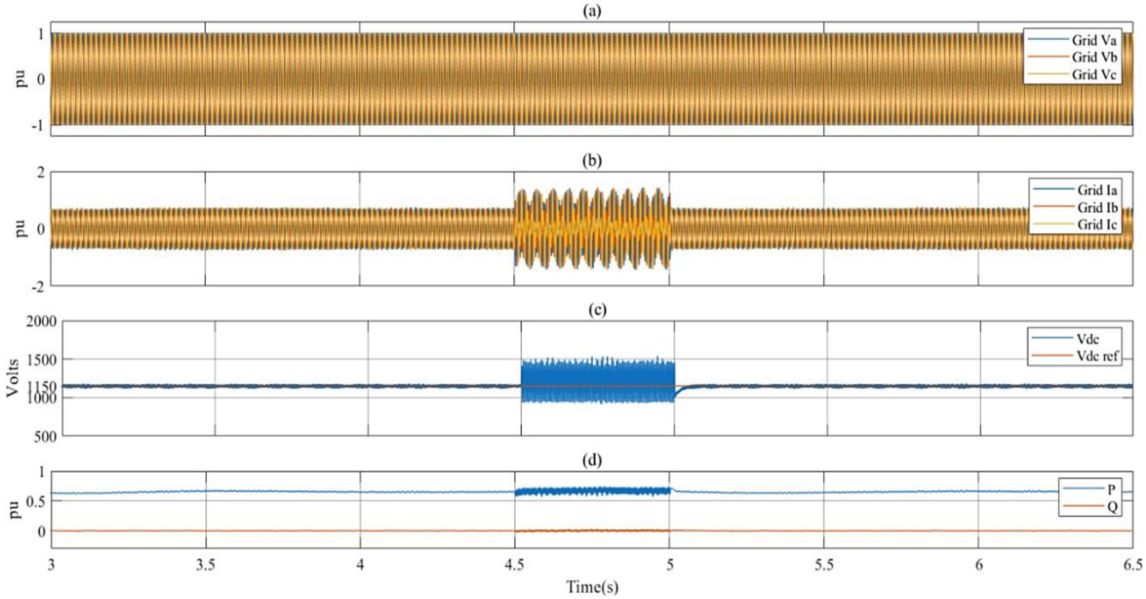

Fig. 5.15. Under Parameter attack (a) Grid side voltage, (b) Grid side current, (c) DC-link voltage and (d) Grid side active and reactive power.

The test results of this malicious attack are shown in Fig. 5.15. The grid side voltage remains constant as shown in Fig. 5.15(a). The outer voltage loop becomes extremely under-damped and unstable, as seen in Fig. 5.15(c). The V_{dc} value starts to oscillate rapidly. As a result, grid current also oscillates as observed in Fig. 5.15(b). This results in oscillations in grid active power (P) and reactive power (Q) as shown in Fig. 5.15(d).

The level of oscillation may vary depending on the severity of the attack rendering shutting down the turbine, this attack makes it a source of instability that may spread to other grid assets.

The Table. 5.3 summaries of all the four cyberattacks modelled and observes the impact of each attack on system variables.

TABLE 5.2: SUMMARY AND IMPACT OF CYBERATTACKS ON PMSG SYSTEM.

Type of attack	Modeling	Observations	Inference
FDI Attack	Add block introduces a constant offset ($\alpha = +1400V$) to the V_{dc} sensor signal.	1. V_{dc} settles to new reference voltage. 2. Small variation in active power (P) and grid current.	Mild Attack
DoS Attack	Switch block redirects the final GSC PWM gate commands to zero at t= 4.5s.	1. V_{dc} shoots to dangerous high level. 2. Instantaneous drop in active power (P) to zero.	Severe Attack
Replay Attack	Switch block redirects the voltage sensor reading to a pre-recorded “normal” voltage at t= 4.5s. A 70% voltage sag occurs at t= 4.51s.	1. V_{dc} rises to dangerous level. 2. Active power (P) sudden rise and fall.	Severe Attack
Parameter Attack	Constant block changes the proportional gain (K_p) of the V_{dc}PI regulator.	1. High-frequency oscillations in V_{dc}. 2. Oscillations in active (P) and reactive (Q) power.	Mild Attack

5.6 CONCLUSION

This chapter presented a comprehensive simulation-based analysis of the PMSG-WECS rigorously evaluating its dynamic performance across normal, abnormal, and cyber-compromised operational states.

First, under normal operating conditions with varying wind speeds, the baseline control schemes demonstrated highly robust performance. The MSC effectively executed MPPT, smoothly ramping up active power generation in direct correlation with the wind profile. Simultaneously, the GSC successfully maintained the DC-link voltage at its reference values which is 1150V and operated at a strict unite power factor.

Second, the system’s performance was evaluated under abnormal grid conditions to test

LVRT capabilities. The results clearly exposed the dynamic limitations of conventional PI based controllers, which struggles to maintain severe voltage sags and only provide LVRT support upto 20% voltage sags. To overcome these challenges, the ANN based LVRT control scheme was introduced which enhances turbine’s physical fault tolerance and LVRT support upto 40%.

This chapter also simulates and analyses the impact of cyber-attacks like FDI, DoS, Replay and Control Parameter attacks on the system. Categorising the attacks from mildly severe to highly severe on based on their impact on the system stability.

Finally, all the findings were simulated using MATLAB/Simulink and validated over real time digital simulation OPAL-RT platform.

CHAPTER 6

CONCLUSION

6.1 OVERALL CONCLUSION

This dissertation systematically investigates the dynamic fault ride through capabilities and cyber physical security of a grid connected PMGS wind energy conversion system. Initial evaluations demonstrated that while conventional PI control schemes are sufficient for normal MPPT, they exhibit severe dynamic limitations under ab normal conditions. The conventional architecture managed a maximum LVRT tolerance only upto 20%. To resolve these vulnerabilities an ANN based LVRT control strategy was developed and implemented for the GSC. The simulation results confirmed that the proposed controller efficiently suppressed DC- link overvoltage, dynamically injected statutory reactive power and by doing so extends the turbine's voltage sag tolerance to 40%.

Furthermore, the detailed cyber-attack studies showed that the conventional controllers are highly vulnerable to FDI, DoS, Replay, and Control Parameter attacks. Malicious manipulation of sensor data easily got past traditional defences, causing dangerous DC-link over voltages, loss of reactive power support, and cascading system instability. Moreover, some of the attacks like FDI and Control Parameter attacks are categorised under mild cyberattacks due to mild oscillation injection into the system whereas the DoS and Replay attacks fall under severe attack category due to highly unstabilizing the system to a dangerous level.

Finally, the computational feasibility and real-world applicability of the proposed control architecture were validated through real time simulation using the OPAL-RT platform. The real time validation closely mirrored the software simulations, definitively proving that intelligent, adaptive control mechanisms are both highly effective and practically viable for securing modern wind energy infrastructure against extreme grid faults.

6.2 FUTURE SCOPE

This dissertation provides a solid foundation for LVRT control and cyber-Attack models, but some promising directions remain for future work:

1. Application of Physics-Informed Neural Networks (PINNs): Future work may investigate the use of PINNs for offline training and real-time control. Embedding the physical governing equations of the PMSG and grid dynamics in the loss function of the neural network can help the control system to achieve faster convergence and better accuracy during the highly stealthy cyber-intrusions.
2. Advanced Adaptive Filtering: The development of dedicated high speed adaptive filtering techniques, such as advanced variants of the Least Mean Square (LMS) algorithm, can be investigated in conjunction with the ANN controller to instantly isolate and neutralize corrupted sensor data before it reaches the converter control loops.
3. Physical Microgrid Integration: Following the successful OPAL-RT validation, the proposed control strategy will be implemented on a scaled physical microgrid test bed with actual PMSG hardware, different energy storage and physical communication networks to investigate the long-term operational wear and thermal stresses during repeated cyber-physical fault scenarios.

APPENDEX

TABLE 5.1: SYSTEM SIMULATION PARAMETERS

Parameter	Value	Description
Wind Turbine		
Rated Power (P_{nom})	4 MW	Nominal mechanical output
Rated Wind Speed	12 m/s	Speed at which rated power is reached
Rotor Radius (R)	54 m	Blade length
Air Density (ρ)	$1.215 kg/m^3$	Standard atmospheric density
Optimal C_p	0.413	Maximum aerodynamic efficiency
Optimal λ	5.6	Optimal Tip Speed Ratio
PMSG		
Stator Resistance (R_s)	0.0223 Ω	Per phase resistance
Stator Inductance ($L_d = L_q$)	$1.35\ mH$	Surface mounted magnets assumed
Flux Linkage (ψ_f)	1.776 Wb	Permanent magnet flux
Pole Pairs (N_p)	60	Allows direct drive operation
DC Link		
DC Voltage (V_{dc})	1150 V	Regulated bus voltage
Capacitor (C_{dc})	0.01 F	Energy buffer
Grid		
Grid Voltage	575 V	Line-to-line RMS
Grid Frequency	50 Hz	Standard frequency
Filter Inductance (L_g)	0.3 H	Grid side filter
Filter Resistance (R_g)	0.03 Ω	Filter damping

REFERENCES

[1] N. Rana, A. Singh, and Shatakshi, "Control and Modelling of PMSG-based Wind Turbine for integration to Conventional Grid," *2025 IEEE North-East India International Energy Conversion Conference and Exhibition (NE-IECCE)*, 2025.

[2] H. Lund, “Renewable energy strategies for sustainable development,” IEEE Trans. Energy Conversion, vol. 32, no. 6, pp. 912–919, Jun. 2007.

[3] Global Wind Energy Council, “Global Wind Report 2023,” IEEE Power and Energy Magazine, vol. 21, no. 2, pp. 102–108, Mar.-Apr. 2023.

[4] S. Heier, Grid Integration of Wind Energy Conversion Systems, IEEE Press, 2014.

[5] Y. Chen, P. Pillay, and A. Khan, “Modelling of doubly-fed induction generator for wind power generator,” IEEE Power Engineering Society General Meeting, vol. 3, pp. 2223–2229, 2005.

[6] L. Holdsworth et al., “Comparison of fixed speed and doubly-fed induction wind turbines during power system disturbances,” IEE Proc. Gener. Transm. Distrib., vol. 150, no. 3, pp. 343–352, 2003.

[7] M. Chinchilla, S. Arnaltes, and J. C. Burgos, “Control of permanent-magnet generators applied to variable-speed wind-energy systems connected to the grid,” IEEE Trans. Energy Conversion, vol. 21, no. 1, pp. 130–135, Mar. 2006.

[8] M. E. Haque, M. Negnevitsky, and K. M. Muttaqi, “A novel control strategy for a variable-speed wind turbine with a permanent-magnet synchronous generator,” IEEE Trans. Industry Applications, vol. 46, no. 1, pp. 331–339, Jan.-Feb. 2010.

[9] M. S. Mahmoud and A. M. A. Zribi, “Modelling and control of variable-speed wind turbines with PMSG,” IEEE Trans. Energy Conversion, vol. 29, no. 1, pp. 20–28, Mar. 2014.

[10] J. Hu et al., “Adaptive sliding-mode control of direct-drive PMSG wind turbines for power maximization under turbulent wind,” IEEE Trans. Industrial Electronics, vol. 60, no. 12, pp. 5983–5991, Dec. 2013.

[11] T. Swibki, I. B. Salem and L. E. Amraoui, "Modeling and control of direct-drive PMSG-based offshore wind turbine under rigorous wind conditions," 2020 6th IEEE International Energy Conference (ENERGYCon), Gammarth, Tunisia, 2020, pp. 62-67, doi: 10.1109/ENERGYCon48941.2020.9236563.

[12] S. Krishnan M, P. G V, S. H. B, A. M S and V. M, "Optimizing the Design and Development of PMSG-based Wind Energy Conversion System," *2024 International Conference on Inventive Computation Technologies (ICICT)*, Lalitpur, Nepal, 2024, pp. 2136-2140, doi: 10.1109/ICICT60155.2024.10544762.

[13] E. Hamatwi et al., “Modelling and control of voltage source converters for grid integration of a wind turbine system,” IEEE PES Power Africa, pp. 98–106, 2016.

[14] S. M. Muyeen et al., “Comparative study on transient stability analysis of wind turbine generator system using different drive train models,” IET Renewable Power Generation, vol. 3, no. 1, pp. 17-27, 2009.

[15] T. Swibki, I. B. Salem, and L. E. Amraoui, "Modeling and control of direct-drive PMSG-based offshore wind turbine under rigorous wind conditions," *2020 6th IEEE International Energy Conference (ENERGYCon)*, pp. 62-67, 2020.

[16] S. Krishnan M, P. G V, S. H. B, A. M S, and V. M, "Optimizing the Design and Development of PMSG-based Wind Energy Conversion System," *2024 International Conference on Inventive Computation Technologies (ICICT)*, pp. 2136-2140, 2024.

[17] E. Muljadi et al., "Low-voltage ride-through capability of a wind plant with a doubly fed induction generator," IEEE Trans. Industry Applications, vol. 47, no. 4, pp. 1761–1767, Jul.-Aug. 2011.

[18] Central Electricity Authority (CEA), "Technical Standards for Connectivity to the Grid," IEEE Power and Energy Society General Meeting, 2020.

[19] N. R. Tummuru, M. K. Mishra, and S. Srinivas, "Dynamic energy management of renewable grid integrated hybrid energy storage system," IEEE Trans. Industrial Electronics, vol. 62, no. 12, pp. 7728–7737, Dec. 2015.

[20] J. Rocabert, A. Luna, F. Blaabjerg, and P. Rodríguez, "Control of Grid-Connected Power Converters during Grid Faults," IEEE Trans. on Industrial Electronics, vol. 58, no. 1, pp. 127-135, Jan. 2011.

[21] C. Wessels, F. Gebhardt, and F. W. Fuchs, "Fault ride-through of a DFIG wind turbine using a dynamic voltage restorer during symmetrical and asymmetrical grid faults," IEEE Trans. on Power Electronics, vol. 26, no. 3, pp. 807-815, March 2011.

[22] S. A. Saleh, R. A. Swief, and A. A. El-Fergany, "ANN-Based Low Voltage Ride-Through Enhancement of Grid-Connected DFIG Wind Turbines," IEEE Access, vol. 7, pp. 119865-119877, 2019.

[23] Hoang, N. N., Trung, H. N., Takano, H., Thanh, S. T., & Tuyen, N. D. (2024). Improved Low Voltage Ride-Through Capability of Permanent Magnet Synchronous Generator Wind Turbine based on Model Predictive Control. *2024 11th International Conference on Power and Energy Systems Engineering (CPESE)*, 21-26.

[24] Makhad, M., Zazi, K., Hilali, A., Loulijat, A., & Marghichi, M. E. (2024). Low Voltage Ride Through Based On Hydrogen Energy Storage for Improving Performance of Wind Energy Conversion System Under Grid Faults. *2024 4th International Conference on Innovative Research in Applied Science, Engineering and Technology (IRASET)*, 1-8.

[25] M, P., Balaraman, S., & P, M. (2024). A New AI Powered Transient Stability Enhancement Scheme for LVRT in Grid-Integrated WPS. *2024 International Conference on Emerging Research in Computational Science (ICERCS)*, 1-8.

[26] A. G. O. et al., "Cyber-Physical Systems Security for the Electric Power Grid," IEEE Transactions on Smart Grid, vol. 8, no. 5, pp. 2454–2461, Sep. 2017.

[27] S. S. Y. L. et al., "A Survey of Cyber-Physical Security Challenges and Solutions for the Modern Power Grid," IEEE Access, vol. 4, pp. 10173–10197, 2016.

[28] E. G. and M. W., "Analysis of the 2015 cyberattack on the Ukrainian power grid," in 2016 IEEE International Conference on Cyber Conflict (CyCon U.S.), Oct. 2016, pp. 1–8.

[29] C. Ozkan, D. Singelée, A. J. Anarjan, R. Loenders and H. Ergun, "Penetration Testing in Wind Farms: Detection and Impact Analysis," *2025 IEEE PES Innovative Smart Grid Technologies Conference Europe (ISGT Europe)*, Valletta, Malta, 2025, pp. 1-5, doi: 10.1109/ISGTEurope64741.2025.11305405.

[30] G. He, Y. Liu, Q. H. Wu and K. Xiahou, "Analysis of Cyber Attacks on Wind Power Generation Systems in Damping Inter-area Oscillations of Power Systems," *2021 IEEE 5th*

Conference on Energy Internet and Energy System Integration (EI2), Taiyuan, China, 2021, pp. 2404-2409, doi: 10.1109/EI252483.2021.9713387.

[31] F. P. A. B. et al., "A MATLAB/Simulink-Based Testbed for Cyber-Attack Simulation on Smart Grid," in 2017 IEEE EEEIC / I&CPS Europe, Jun. 2017, pp. 1–6.

[32] K. Yang, J. Li, G. Zhang, Y. Xing, O. Bamisile and Q. Huang, "A Cooperative Control Strategy against Cyber-attacks for Power System with High Penetration Wind Farm," *2022 4th Asia Energy and Electrical Engineering Symposium (AEEES)*, Chengdu, China, 2022, pp. 321-327, doi: 10.1109/AEEES54426.2022.9759822.

[33] Z. J. J. Zhang, Z. Zeng, J. Pan and M. Saeedifard, "A Cyber-Attack Targeting HVDC-Connected Offshore Wind Farms Considering Stability of Grid-Following Power Converters," *2024 IEEE Energy Conversion Congress and Exposition (ECCE)*, Phoenix, AZ, USA, 2024, pp. 1667-1674, doi: 10.1109/ECCE55643.2024.10861375.

[34] Wu, H., Badihi, H., Xue, Y., & Vilkko, M. (2024). A Normal Behavior Model Based on Machine Learning for Wind Turbine Cyber-Attack Detection. *2024 International Workshop on Artificial Intelligence and Machine Learning for Energy Transformation (AIE)*, 1-6.

[35] Z. Chen, J. Zhu, S. Li and T. Luo, "Detection of False Data Injection Attack in Automatic Generation Control System with Wind Energy based on Fuzzy Support Vector Machine," *IECON 2020 The 46th Annual Conference of the IEEE Industrial Electronics Society*, Singapore, 2020, pp. 3523-3528, doi: 10.1109/IECON43393.2020.9255020.

[36] S. Zhao, Q. Yang, P. Cheng, R. Deng and J. Xia, "Adaptive Resilient Control for Variable-Speed Wind Turbines Against False Data Injection Attacks," in *IEEE Transactions on Sustainable Energy*, vol. 13, no. 2, pp. 971-985, April 2022, doi: 10.1109/TSTE.2022.3141766.

[37] M. A. Taher, H. Iqbal, M. Tariq and A. I. Sarwat, "Disruptive Effects of Denial-of-Service (DoS)Attacks on Microgrid Distributed Control: Altered Communication Topology, Voltage Stability, and Accurate Power Allocation," *2023 IEEE International Conference on Energy Technologies for Future Grids (ETFG)*, Wollongong, Australia, 2023, pp. 1-6, doi: 10.1109/ETFG55873.2023.10407127.

[38] M. M. S. E. K., "A stealthy 'replay' attack on a power system with its analysis and countermeasures," in 2014 IEEE International Conference on Smart Grid Communications (SmartGridComm), Nov. 2014, pp. 524–529.

[39] P. K. Vidyarthi, A. Kumar and R. Shankar, "Different Types of Cyber-Attacks on Microgrid and its Detection and Mitigation," *2024 IEEE 4th International Conference on Sustainable Energy and Future Electric Transportation (SEFET)*, Hyderabad, India, 2024, pp. 1-5, doi: 10.1109/SEFET61574.2024.10718222.

LIST OF PUBLICATIONS

1. N. Rana, A. Singh and Shatakshi, "Control and Modelling of PMSG-Based Wind Turbine for Integration to Conventional Grid," *2025 IEEE North-East India International Energy Conversion Conference and Exhibition (NE-IECCE)*, Silchar, India, 2025, pp. 1-6, doi: 10.1109/NE-IECCE64154.2025.11183170. (Scopus Indexed).
2. Accepted and Presented; N. Rana, A. Singh and Shatakshi, "(Analysis of Different Cyberattacks on PMSG-Based Wind Turbine Control Systems," *2026 IEEE 1st International Conference on Intelligent Computing and Automation for Sustainable Solutions (ICASS)*, Faridabad, India, 12th 13th February, 2026.

PAPER ACCEPTANCE PROOF

NE-IECCE2025/P-613

2025 IEEE North-East India International Energy Conversion Conference and Exhibition
(NE-IECCE 2025)
4-6 July, 2025
National Institute of Technology Silchar, Assam, India

Certificate of Participation

This is to certify that the paper entitled

Control and Modelling of PMSG-based Wind Turbine for integration to Conventional Grid Authored by **Nischay Rana, Alka Singh, Shatakshi** in the IEEE international Conference on " North East India International Energy Conversion Conference and Exhibition" **(NE-IECCE 2025),** Organized by **IEEE IAS Joint Chapter Silchar Subsection** in collaboration with Electrical Engineering Department, National Institute of Technology Silchar (NIT Silchar), During **04th July – 06th July 2025** at NIT SIlchar, Assam, India.

Dr. Amritesh Kumar
Organizing Chair
NE-IECCE 2025

Dr. Asha Rani MA
Organizing Chair
NE-IECCE 2025

Dr. Vinod Khadkikar
General Chair
NE-IECCE 2025

Prof. B. K. Roy
Chair
IEEE Silchar Subsection

1st International Conference on
Intelligent Computing and Automation for Sustainable Solutions
(ICASS-2026) Conference Record #69550
12th – 13th February, 2026

Certificate of Participation

This is to certify that

NISCHAY RANA

Presented a Paper

Analysis of Different cyber attacks on PMSG- Based wind
Turbine control systems

in 1st International Conference on Intelligent Computing and Automation for Sustainable Solutions (ICASS-2026) organized by School of Engineering, Manav Rachna University on 12th–13th February, 2026

Dipali
Prof.(Dr.) Dipali Bansal
General Chair, ICASS-2026
Dean, School of Engineering, Manav Rachna University

Prof. (Dr.) Deependra Kumar Jha
Vice Chancellor,
Manav Rachna University

Control and Modelling of PMSG-based Wind Turbine for integration to Conventional Grid

Nischay Rana
Dept. of Electrical Engineering
Delhi Technological University
Delhi, India
nischayk12@gmail.com

Alka Singh
Dept. of Electrical Engineering
Delhi Technological University
Delhi, India
alkasingh.eed@gmail.com

Shatakshi
Dept. of Electrical Engineering
Delhi Technological University
Delhi, India
shatakshi@dtu.ac.in

2025 IEEE North-East India International Energy Conversion Conference and Exhibition (NE-IECCE) | 979-8-3315-1061-9/25/$31.00 ©2025 IEEE | DOI: 10.1109/NE-IECCE64154.2025.11183170

***Abstract*— This research paper shows the modelling of PMSG based wind turbine model and its control scheme. The machine side control uses Field oriented control (FOC) technique as an MPPT technique, to extract maximum power output from the wind turbine. The speed of wind is considered as a step function changing with time. Voltage-oriented control (VOC) is used at the grid side controller. The control and modelling have been performed on MATLAB/Simulink 2024a and results are taken to analyze the system performance and effectiveness.**

Keywords*— *Wind energy, FOC, Modelling, VOC, MPPT, PMSG, Wind turbine.

I. INTRODUCTION

Advancing technology has given rise to high power demand. It is also well known that meeting the daily power requirement requires a lot of fossil fuels (like oil, gas, and coal) but these are getting exhausted in nature, leading to global warming and environmental pollution [1-2]. Renewable energy integration to the regional grids is the best way to reduce the carbon footprint in our environment and making it clean. Commonly employed renewable energy sources are solar, wind, ocean. Work on integrating these renewable sources into the conventional grid is taking place on a very high pace. Solar integration has already made a lot of advancement and now the wind energy utilization is on the rise due to its cost competitiveness as compared to the other conventional energy resources [3-6]. The data analyzed from Global Wind Energy Council (GWEC) in its report for the year 2023 has shown that in 2023 alone the total wind installations amounted to 117GW. The wind power has grown to 1000GW by the end of year 2024 including offshore and onshore wind turbines and the wind energy is now contributing 10% of electricity worldwide. Some of the popular global manufacturers of wind turbines are Goldwind, Suzlon Energy, Vestas, Siemens Gamesa Renewable Energy, GE Vernova.

Wind turbines may be classified into two main categories: Fixed-speed and Variable speed wind turbines [7]. Fixed-speed wind turbines can only extract the maximum power at rated speed and fail to extract the maximum power at different wind speed [8-9]. Whereas, variable speed turbines are capable of extracting the maximum power under variable speed conditions. Variable speed turbines are more efficient than fixed-speed turbines and are hence preferred. Variable speed wind turbines are also sub classified on the basis of generator: Doubly-Fed Induction Generator (DFIG) and Permanent Magnet Synchronous Generator (PMSG) [10-12]. Furthermore, many research works have investigated the control techniques of wind turbines. Most of the studies are based on DFIG wind turbines. However, DFIG based turbines require a high maintenance cost due to the gearbox and slip rings requirement. Moreover, the performance of this type of turbine reduces under low wind conditions. Hence the PMSG wind turbines are preferred over DFIG [12-15].

In this paper, we will discuss the modelling and control of 4 MW wind turbine based on PMSG, the dc link of this machine is rated at 1150V. This paper discusses the detailed control of the grid side controller and machine side controller. Two converters have been used one as a Grid side control (GSC) which works as inverter and the other as a machine side control (MSC) which works as rectifier. At the grid side a resistance-inductor filter is used reduce harmonics and ripples and the grid. MSC contains MPPT controller, pitch angle controller.

The paper is organized into following manner. Section II discusses modelling of wind turbine and PMSG, Section III discusses the Control Schemes Modelling of GSC and MSC, Section IV depicts results and simulation, while the Conclusion is shown in Section V.

II. MATHAMATICAL MODELING OF SYSTEM

A. Modelling of Wind Turbine

Wind turbine chosen for the modelling is PMSG based turbine due to its light weight and better performance under different wind conditions over the other as mentioned in the literature. Fig.1 depicts the PMSG based wind energy integration system. The output power P_m of wind turbine is a function of the wind velocity v and is expressed as:

$$P_m = \frac{1}{2}\rho A C_p(\lambda, \beta) v^3 \tag{1}$$

where, A is the area of rotor blades (m^2), ($A = \pi R^2$, R is the radius of rotor blades (m^2)), v is the wind speed (m/s) and $C_p(\lambda, \beta)$ is the power coefficient, ρ is air density equal to 1.215kg/m².

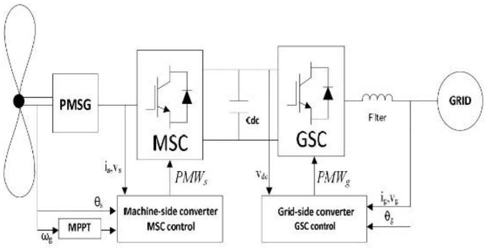

Fig.1. Wind energy integration system diagram.

979-8-3315-1061-9/25/$31.00 ©2025 IEEE

Analysis of Different Cyberattacks on PMSG-Based Wind Turbine Control Systems

Nischay Rana
Dept. of Electrical Engineering
Delhi Technological University
Delhi, India
nischayk12@gmail.com

Alka Singh
Dept. of Electrical Engineering
Delhi Technological University
Delhi, India
alkasingh.eed@gmail.com

Shatakshi
Dept. of Electrical Engineering
Delhi Technological University
Delhi, India
shatakshi@dtu.ac.in

***Abstract*— Advanced control and communication networks have made it easier to integrate renewable energy sources, especially wind energy, into the power grid. Although efficiency is increased, but there are sever cybersecurity risks too. The cyber-physical security of Permanent Magnet Synchronous Generator (PMSG) wind turbine connected to the grid is studied in this paper. The turbine along with its converter system and other controllers are all represented by suitable models created in MATLAB/Simulink. A variety of cyberattacks are then simulated using this model as a testbed, such as false data injection (FDI), denial-of-service (DoS) attacks on converter commands, replay attacks on grid measurements and direct parameter attacks on controller logic on vital sensors. Each attack's dynamic effects on important system states, including DC-link voltage, active/reactive power output, and system stability are examined. The findings show that these attacks can effectively destabilize the turbine, interfere with power generation and in extreme cases, impair the system's defences and may result in catastrophic failure.**

Keywords*— *cyber-physical systems, PMSG, wind turbine, cyber-security, false data injection, denial-of-service.

I. INTRODUCTION

The need for decarbonization and the phenomenal growth of Distributed Energy Resources (DERs) is causing a fundamental shift in the world's electrical grids. Focus has shifted to wind energy [1], especially toward Permanent Magnet Synchronous Generator (PMSG) turbines, due to their cost-effectiveness and improved power output as compared to other generators like Doubly-Fed Induction Generator (DFIG) [2].

Advanced power-electronic control is achievable through their high efficiency and full converter-based grid decoupling. However, these systems are complex Cyber-Physical Systems (CPS) which combine real-time controllers, communication networks (like SCADA), and a deep layer of sensors with physical components [3].

A new and hazardous attack surface is produced by this digitization. In contrast to conventional IT systems, a cyberattack on the operational technology (OT) of a power system has the potential to spread from the virtual realm into the real world, resulting in widespread blackouts, equipment damage, and financial loss [4]. A clear example of this threat was the 2015 attack on the Ukraine power grid [5].

Although there has been research on cybersecurity at the grid level [6], there is increasing concern about the vulnerabilities of inverter-based resources, such as PMSG wind turbines [7,8]. The authenticity, availability, and integrity of sensor data and command signals are critical components of their intricate, fast control loops. Without being noticed by traditional security measures, an attacker who is aware of these control loops can perform surgical strikes to destabilize the asset [9,10].

This paper offers a thorough dynamic analysis of numerous cyberattacks on a high-fidelity PMSG wind turbine model, this study emphasizes the need of anomaly detection system and the need of resilient control mechanism. This work's main contributions relate to modelling and simulation of four unique and sophisticated cyberattack vectors: False Data Injection (FDI) [11,12], Denial-of-Service (DoS) [13], Replay [14], and Control Parameter attack [15], followed by implementation of a comprehensive PMSG based wind turbine control system is modeled in MATLAB/Simulink to function as a single simulation testbed. This research discusses the quantitative evaluation of each attack on the turbine's operational performance, stability and serves as a baseline for advanced control mechanisms.

This paper is structured as follows: Section II consists of control and modeling of PMSG based wind turbine system. The attack formulations are shown in Section III. Section IV covers the simulation results and analysis for each attack scenario. Section V finally concludes the paper.

II. MODELING AND CONTROL OF PMSG SYSTEM

The benchmark system is a grid-connected PMSG wind turbine. According to Fig. 1, the PMSG, a back-to-back (B2B) full-scale converter, a DC link capacitor, and resistive-inductive filter for grid interfacing make up the system's architecture. The details of PMSG system are mentioned in Appendix.

A DC link interfaces the Grid-Side Converter (GSC) and the Machine-Side Converter (MSC), which together make up the B2B converter. The hierarchical control system, depicted in Fig. 1, oversees the turbine's overall operation.

A. Wind Turbine Modelling

The wind turbine selected for the modelling is the PMSG-based turbine, due to its better performance under low and different wind conditions, light weight, and lower maintenance cost than the others, as mentioned in the literature [2]. Fig. 1, represents the overall system block diagram of a PMSG-based wind energy integration system.

The output power P_n of wind turbine is expressed as:

$$P_n = \frac{1}{2}\rho A C_p(\lambda, \beta) v^3 \qquad (1)$$

where v is speed of the wind (m/s), A is the rotor blades area (m^2), ρ is density of air and $C_p(\lambda, \beta)$ is the power coefficient.